Chemical Physics 230 (1998) 153–186

Chemical Physics

Valence orbital electron momentum distributions for oxygen: comparison of EMS measurements with theory

J. Rolke [a], Y. Zheng [a], C.E. Brion [a,*], Y.A. Wang [b,1], E.R. Davidson [b]

[a] Department of Chemistry, University of British Columbia, 2036 Main Mall, Vancouver, BC, Canada V6T 1Z1
[b] Department of Chemistry, Indiana University, Bloomington, IN 47405, USA

Received 16 September 1997; in final form 21 December 1997

Abstract

The valence shell binding energy spectra and orbital electron momentum profiles of O_2 have been measured by energy dispersive multichannel electron momentum spectroscopy at an impact energy of 1200 eV + binding energy. The effects of electron correlation on the valence binding energy spectrum are investigated using multi-reference singles and doubles configuration interaction calculations. The presently reported experimental momentum profiles of O_2 display considerably improved statistics compared with previously published EMS results. The measured momentum profiles are compared with cross sections calculated using both unrestricted and restricted open shell Hartree–Fock methods with basis sets ranging from minimal to near Hartree–Fock limit in quality. In addition, the effects of correlation and relaxation on the calculated momentum profiles are investigated using multi-reference singles and doubles configuration interaction calculations of the full ion-neutral overlap distributions. Electron correlation effects in the ground state are further examined using several density functional approaches for the momentum profiles. The present EMS measurements and MRSD-CI calculations clearly show that the binding energy peak at ~27.3 eV has significant contributions from both $^4\Sigma_u^-$ and $^2\Sigma_u^-$ processes in contrast to earlier assignments which have attributed this peak to the $C\,^2\Sigma_u^-$ state alone. Similarly, the binding energy peak at 33 eV is shown to be due to $^2\Sigma_u^-$ rather than earlier assignments of $^2\Pi_u$ character. © 1998 Elsevier Science B.V. All rights reserved.

1. Introduction

The electronic structure of the oxygen molecule has been the subject of many theoretical and experimental studies. This interest is due in part to the great abundance of the molecule and to the important role it plays in living systems and in atmospheric processes [1]. The open-shell nature of O_2 adds a challenging aspect to quantum mechanical calculations that is not present for closed-shell molecules. Experimentally, He I and He II experiments [2–6] using high-resolution photoelectron spectroscopy (PES) for the valence shell ionization processes of O_2 have been reported up to ~28 eV binding energy. Gardner and Samson [7] extended the

---

[*] Corresponding author.

[1] Present address: Dept. of Chemistry, University of California at Los Angeles, Los Angeles, CA 90095-1569 USA.

PII S0301-0104(98)00012-3

valence shell He II PES studies to ∼40 eV binding energy and high resolution threshold PES studies using synchrotron radiation have also been reported [8]. In addition, X-ray photoelectron spectroscopy (XPS) studies up to ∼32 [9] and ∼60 eV [10] have been reported. The full valence shell binding energy spectrum has also been measured at low resolution (1 eV fwhm) by dipole (e,2e) spectroscopy [11] and by electron momentum spectroscopy (2 eV fwhm) [12] out to ∼60 eV.

Electron momentum spectroscopy (EMS) with symmetric non-coplanar geometry provides detailed information on the electronic structures of atoms and molecules [13–16] and in particular measures orbital electron densities (momentum distributions). In the EMS reaction, the kinematics of the electrons are completely determined and, under these conditions, the reaction provides two categories of information. Firstly, the binding energy spectra are obtained over a wide energy range by keeping the energies of the emitted electrons equal and fixed and varying the incident energy. Secondly, for the transitions giving rise to the peaks in the binding energy spectrum, the electron momentum distribution for the molecular orbital characteristic of the initial state in the transition is obtained to within a close approximation by measuring the EMS cross-section at a fixed binding energy ϵ as a function of the azimuthal angle ϕ between the detectors for the two emitted electrons. Consequently, the EMS technique provides stringent tests for quantum chemical calculations at the Hartree–Fock (HF), configuration interaction (CI) and density functional theory (DFT) levels. In addition, the EMS technique is particularly sensitive to the chemically important outer spatial (low momentum) regions of the electron density in the molecule [14].

The first reported study of O_2 by EMS was the early single channel experimental work of Suzuki et al. [12] in which valence electron momentum distributions corresponding to the major features in the binding energy spectrum up to 60 eV were obtained. While no calculated binding energy spectra or theoretical momentum profiles were reported in that work [12], experimental momentum profiles were obtained for binding energies up to 60 eV. In some cases, the experimental momentum profiles corresponding to the production of the individual quartet and doublet ion states arising from ionization of the same orbital were obtained. The $a^4\Pi_u$ and $A^2\Pi_u$ ion states were difficult to deconvolute because of the limited statistics even with the higher energy resolution (1.2 eV fwhm) available at impact energies of 400 eV. In addition, the $1\pi_u$ ionization satellite peak at 23.7 eV could not be resolved from the nearby $c^4\Sigma_u^-$ state. On the basis of the shapes of the observed momentum profiles, the peaks at 39 and 47 eV were assigned to $^4\Sigma_g^-$ and $^2\Sigma_g^-$ ion states from $2\sigma_g$ ionization although no accounting for the total $2\sigma_g$ pole strength and the high binding energy region out to 60 eV was made. A further limitation was the statistical precision of the data due to low instrumental sensitivities [12]. In particular, the momentum profiles corresponding to the $C^2\Sigma_u^-$ and 33.0 eV final ion states showed large scatter [12].

Subsequent EMS work on O_2 by Tossell et al. [17] presented both experimental and theoretical momentum profiles for the five valence orbitals of O_2 but no binding energy spectra were reported. However, although the shapes of the observed momentum profiles agreed qualitatively with theory, the calculations used very limited basis set size [17]. Very limited statistics were also apparent and the momentum profiles corresponding to individual quartet and doublet states were not resolved [17].

The binding energy spectra of oxygen are more complex than for closed-shell cases because of the presence of both quartet and doublet final ion states which make the deconvolution and interpretation of the spectra more difficult. The ability of theory to predict the relative intensity of the quartet and doublet ion states in the EMS spectrum of oxygen (or other open-shell molecules) and their corresponding momentum profiles has not been investigated.

The initial orbital origin of the peak in the 33 eV region of the O_2 binding energy spectrum has been the subject of considerable dispute. Gardner and Samson [7] did not include this energy region in their experiment while the XPS study of Siegbahn et al. [10] attributed the 33 eV peak to shake-up or more likely characteristic energy losses. The fact that the peak was observed at a comparable intensity in dipole (e,2e) work [11], which was done at much lower pressure than the XPS study [10], suggested that energy losses undergone by ejected photoelectrons could be ruled out and that the peak at 33 eV was more likely due to final ion states arising from shake-up mechanisms. The propagator techniques used by Cederbaum and Domcke [18] calculated all of the $^2\Pi_u$

intensity to be at energies ≤ 27.3 eV while Dixon and Hull [19] predicted all the ${}^2\Pi_u$ intensity to be at ≤ 22.7 eV. Other theory by Honjou et al. [20,21], using configuration interaction wavefunctions placed all of the ${}^2\Pi_u$ intensity at energies ≤ 24.3 eV and predicted that the peak at 33.0 eV was mainly due to ${}^2\Sigma_u^-$ and (to a lesser extent) ${}^2\Sigma_g^-$ poles. The multiconfigurational electron propagator calculations of Yeager and co-workers [22,23] predicted that almost all the intensity due to ionization of a $1\pi_u$ electron is below 24.56 eV and also indicated that a transition at ~ 34.7 eV is due to a ${}^2\Sigma_u^-$ state. The electron propagator techniques by Purvis and Öhrn [24] did not predict any poles in the 33 eV region. Gerwer et al. [25] suggested that the 33 eV peak be assigned as ${}^2\Pi_u$ since this led to reasonable agreement between their calculated total electronic ion state cross-sections for formation of $(1\pi_u)^{-1}$ ions and those obtained by measurements using dipole (e,2e) spectroscopy [11] as well as He I PES experiments using a many line light source [26]. However, many corrections were required [25] for unresolved experimental final ion state cross-sections and the agreement between theory and experiment was only moderately good. On the basis of the observed p-type momentum profile and peak area arguments, Suzuki et al. [12] suggested that the peak at 33 eV was due to a ${}^2\Pi_u$ satellite associated with the $1\pi_u$ ionization process. However, this assignment [12] was not definitive since poles from $2\sigma_u$ ionization with $c^4\Sigma_u^-$ or $C^2\Sigma_u^-$ parent final ion states would also have p-type momentum distributions similar to those from poles corresponding to ${}^2\Pi_u$ ionic states. No momentum profiles were reported for the 33 eV region in the EMS work of Tossell et al. [17].

The above history indicates that improved experimental and more detailed theoretical investigations of O_2 are desirable. In the intervening years since the previous EMS studies on O_2 [12,17] large improvements in sensitivity have been achieved with the development of multichannel EMS spectrometers [27–29]. In addition, a range of much more sophisticated calculation methods using large basis sets are now possible with current computing devices. Recent work on open shell molecules in this laboratory [30] has presented more detailed theoretical calculations and multichannel EMS experimental work for the outermost (HOMO) orbital of O_2 as well as for NO and NO_2. The present work now reports multichannel energy dispersive electron momentum spectroscopy measurements of all valence orbital momentum profiles and complete valence shell binding energy spectra (up to 59 eV) for O_2 with improved statistical precision compared with previous work. The comparison of theoretical intensities to the experimental EMS binding energy spectrum and the subsequent theoretical modelling of the measured momentum profile intensities has also been carried out using a range of computational methods and basis sets. The EMS binding energy spectra including the more complex inner valence region are compared with the results of a new multi-reference singles and doubles configuration interaction (MRSD-CI) calculation of the ionic states using very large basis sets. The measured orbital momentum profiles are compared with a variety of Hartree–Fock treatments ranging from a minimal STO-3G basis to near Hartree–Fock limit quality basis sets including a 168 contracted Gaussian type orbital (168-GTO) calculation developed in the course of the present collaborative work. Both the unrestricted Hartree–Fock (UHF) and restricted open-shell Hartree–Fock (ROHF) methods have been used to calculate momentum profiles in the present work. In addition, the effects of correlation and electronic relaxation on all of the valence orbital momentum profiles are also investigated with new MRSD-CI overlap calculations (168-G(CI)). In the case of the outermost $1\pi_g$ orbital (${}^2\Pi_g$ final ion state) an averaged coupled-pair functional (ACPF) [31] calculation using the 168-GTO basis is also reported. Many-electron effects on all O_2 momentum profiles are further investigated with density functional methods, using the target Kohn–Sham approximation of the EMS cross-section [29,30,32–39] with local and non-local (gradient corrected) functionals.

In the present work, careful attention has also been given to obtaining individual experimental momentum profile measurements corresponding to the separate quartet and doublet final ion state exit channels arising from a common initial orbital origin. Experimental momentum profiles are provided for all of the orbital ionizations leading to the $X\,{}^2\Pi_g$, $a^4\Pi_u$, $A^2\Pi_u$, $b^4\Sigma_g^-$, $B^2\Sigma_g^-$, ${}^2\Pi_u(3)$, $c^4\Sigma_u^-$ and $C^2\Sigma_u^-$ final ion states as well as for the peak at 33 eV. The inner valence $2\sigma_g$ ionization (${}^4\Sigma_g^-$ and ${}^2\Sigma_g^-$ final ion states) pole strengths have been studied by an analysis of the binding energy and momentum profiles for the high energy 36–59 eV region. The comparison of the calculated momentum profiles with individual experimental momentum profiles has been used to determine pole strengths for the $1\pi_u$ ionization peaks corresponding to the $A^2\Pi_u$ parent state and the ${}^2\Pi_u(3)$

satellite state (23.7 eV) and these pole strengths have been compared with previously published experimental [3,12] and theoretical [18–25] results. In a similar way, pole strengths for production of the $c^4\Sigma_u^-$ and $C^2\Sigma_u^-$ states from $2\sigma_u$ ionization have also been determined. An assignment of the peak at 33 eV in the binding energy spectra is provided by an analysis of the measured EMS and calculated MRSD-CI binding energy spectra and the pole strengths in the $(1\pi_u)^{-1}$ and $(2\sigma_u)^{-1}$ manifolds.

2. Experimental method

The symmetric non-coplanar energy dispersive multichannel EMS spectrometer has been described in detail [29] and thus only a brief description will be given here. The gas-phase target molecules ($\sim 10^{-5}$ Torr) are ionized by impact with a high energy electron beam ($E_0 = 1200$ eV + binding energy). The outgoing electrons (scattered and ionized) are electron optically retarded to 50 eV, selected energetically by electrostatic analyzers and detected in coincidence.

In the symmetric non-coplanar scattering geometry, the two outgoing electrons are selected to have equal polar angles ($\theta_1 = \theta_2 = 45°$) relative to the forward scattered electron beam. Each electron energy analyzer accepts a range of kinetic energies from 596 to 604 eV simultaneously, but only those coincident electron pairs with summed energies in the range of 1200 ± 3.5 eV are recorded [29]. The relative azimuthal (out of plane) angle ϕ between the two outgoing electrons is variable over the range of 0° to $\pm 30°$. Under these high impact energy and high momentum transfer conditions, the plane wave impulse approximation (PWIA) provides a good description of the collision [15] and the ionized electron essentially undergoes a clean ‘knock-out’ collision. In the PWIA, the momentum p of the ejected electron prior to knock-out is related to the azimuthal angle by [13,15]:

$$p = \left[(2p_1 \cos\theta_1 - p_0)^2 + (2p_1 \sin\theta_1 \sin(\phi/2))^2 \right]^{1/2} \tag{1}$$

where $p_1 = p_2 = \sqrt{2E_1}$ is the magnitude of the momentum of each outgoing electron and $p_0 = \sqrt{2E_0}$ is the momentum of the incident electron (both in atomic units).

In EMS the individual orbitals are selected according to their binding (or ionization) energies. With the multichannel energy dispersive spectrometer used in the present work, binding energy spectra (BES) are collected at a series of azimuthal angles ϕ. Momentum distributions as a function of angle are obtained by deconvolution of these binding energy spectra using Gaussian functions located at each ionization energy in the BES. The widths of the Gaussian functions can be determined from a consideration of published PES vibronic manifolds and the instrumental energy resolution function (1.5 eV fwhm). For each ionization process, the area of the fitted peak (or the integral of the spectral region, where appropriate) is plotted as a function of momentum (calculated from ϕ using Eq. (1)). The set of areas as a function of momentum for a specific binding energy is referred to as an experimental momentum profile (XMP). All multichannel measurements in the present work were obtained using the ‘binning’ mode [29]. The O_2 sample was obtained from Medigas gas products and was of $> 99.0\%$ purity. No impurities were observed in any of the spectra.

3. Theory

3.1. Cross-sections calculated using spin unrestricted open shell EMS theory

The EMS binary (e,2e) differential cross-section *per electron* in the PWIA for randomly oriented gas-phase molecules is given by [13–15,37]:

$$\sigma_{EMS} \propto \sum_f \left[S_f^2 \int |\langle \boldsymbol{p} \Psi_f^{N-1} | \Psi_i^N \rangle|^2 \, d\Omega \right] \tag{2}$$

where $\boldsymbol{p}$ is the momentum of the target electron state prior to knockout and $|\Psi_f^{N-1}\rangle$ and $|\Psi_i^N\rangle$ are the total electronic wavefunctions for the final ion state and the target molecule ground (initial) state respectively. It should also be noted that Eq. (2) involves both initial and final state correlation and the quantity S_f^2 is as defined in Ref. [37]. The overlap of the ion and neutral wavefunctions in Eq. (2) is known as the Dyson orbital while the square of this quantity is $|\langle \boldsymbol{p}\Psi_f^{N-1}|\Psi_i^N\rangle|^2$ and is referred to as an ion-neutral overlap distribution (OVD). Thus, the EMS cross section is essentially proportional to sums of spherical averages of the squares of the Dyson orbitals in momentum space. This generalized formulation of the EMS cross-section is useful when using many-body calculations for the initial and final wavefunctions, such as configuration interaction treatments [14,15,37,40]. The summation in Eq. (2) is over all degenerate final state wavefunctions corresponding to the same experimental binding energy. This formulation with the summation is appropriate for unrestricted open shell calculations for systems such as O_2.

Eq. (2) is greatly simplified by using the Target Hartree–Fock approximation (THFA). Within the THFA, only final (ion) state correlation is allowed [37] and the many-body wavefunctions $|\Psi_f^{N-1}\rangle$ and $|\Psi_f^N\rangle$ are approximated as independent particle determinants of ground state target Hartree–Fock orbitals. In the THFA, $S_f^2 = S_j^f$, as can be seen from Ref. [37]. The quantity S_j^f is called the spectroscopic factor and is the probability of the ionization event producing a $(\Psi_j)^{-1}$ one-hole configuration of the final ion state, $|\Psi_f^{N-1}\rangle$. The ion state is then dominated by a single hole in only one orbital and Eq. (2) can be simplified to:

$$\sigma_{\mathrm{EMS}} \propto \sum_f S_j^f \int |\psi_j(\boldsymbol{p})\,\alpha|^2 \,\mathrm{d}\Omega + \sum_f S_j^f \int |\psi_j(\boldsymbol{p})\,\beta|^2 \,\mathrm{d}\Omega \tag{3}$$

where $\psi_j(\boldsymbol{p})$ is the one-electron momentum space canonical Hartree–Fock orbital wavefunction for the jth electron, corresponding to the orbital from which the electron was ionized. The quantity $\psi_j(\boldsymbol{p})$ is the Fourier transform of the more familiar one-electron position space orbital wavefunction $\psi_j(\boldsymbol{r})$. The integrals in Eq. (3) are known as the spherically averaged one-electron momentum distributions (MDs).

Eq. (2) may also be re-interpreted in the context of Kohn–Sham density functional theory [33,34]. The Target Kohn–Sham Approximation (TKSA) gives a result similar to Eq. (3) in which the canonical Hartree–Fock orbital is replaced by a momentum space Kohn–Sham orbital $\psi_j^{\mathrm{KS}}(\boldsymbol{p})$:

$$\sigma_{\mathrm{EMS}} \propto \sum_f \int |\psi_j^{KS}(\boldsymbol{p})\,\alpha|^2 \,\mathrm{d}\Omega + \sum_f \int |\psi_j^{KS}(\boldsymbol{p})\,\beta|^2 \,\mathrm{d}\Omega \tag{4}$$

It should be noted that some accounting of electron correlation effects in the target ground state is included in the TKSA via the exchange correlation potential. A more detailed description of the TKSA-DFT method may be found elsewhere [33,34]. The TKSA approach has been compared with near Hartree–Fock limit and MRSD-CI overlap calculations and EMS measurements for the experimental momentum profiles of a number of small molecules [30,33,37] including HOMOs of O_2, NO and NO_2 [30] as well as to large molecules [29,32,35,36,38,39].

To compare the cross-sections calculated as a function of momentum using Eqs. (2)–(4) above with the measured XMPs, the effects of the finite spectrometer acceptance angles in both θ and ϕ ($\Delta\theta = \pm 0.6°$ and $\Delta\phi = \pm 1.2°$) must be included in the TMPs. This is achieved in the present work using the Gaussian-weighted planar grid method of Duffy et al. [41]. After momentum resolution folding, the OVD (Eq. (2)) or the MDs (Eqs. (3) and (4)) are referred to as theoretical momentum profiles (TMPs).

The specific forms of Eqs. (2)–(4) above have been determined in the present work for spin-unrestricted descriptions of the electronic structure of O_2 (see Appendix A for the case of the THFA form of Eq. (3)). In the case of the HOMO of O_2 only an α electron may be ionized (to give the $^2\Pi_g$ state of O_2^+) so that the calculation is straightforward (i.e. Eq. (2) has only one term and Eqs. (3) and (4) retain only the term involving $\psi_j(\boldsymbol{p})\alpha$ or $\psi_j^{\mathrm{KS}}(\boldsymbol{p})\alpha$, respectively). In addition, it should be remembered that the resulting cross-section for the HOMO is per electron (i.e. in the case of the doubly occupied HOMO of O_2 the relative cross-section must be doubled).

The situation is rather different if an orbital other than the $1\pi_g$ (HOMO) orbital is ionized. In cases where a quartet final ion state is produced, then the ion state spin eigenfunction must result in a total spin of 3/2 [2]. One possible spin eigenfunction corresponds to the $\alpha(1)\alpha(2)\alpha(3)$ configuration for the three unpaired electrons in the ion. In this case it can be said that a $\psi_j\beta$ electron ionization process from the orbital of interest contributes to the spin unrestricted TMP corresponding to the quartet ion state. However, as shown in Appendix A, a spin eigenfunction with total spin of 3/2 can also be constructed from a particular linear combination of the $\alpha(1)\alpha(2)\beta(3)$, $\alpha(1)\beta(2)\alpha(3)$ and $\beta(1)\alpha(2)\alpha(3)$ electron configurations for the ion. Thus, $\psi_j\alpha$ electron ionization from the orbital of interest also makes a contribution to the spin-unrestricted TMP corresponding to the quartet final ion state. The relative contributions of these $\psi_j\beta$ and $\psi_j\alpha$ electron ionizations to the spin unrestricted TMPs corresponding to a quartet ion state of O_2 are 1 and 1/3, respectively (see Appendix A). Similarly, for ionization from an orbital (other than the HOMO) producing a doublet final ion state, the ion state spin eigenfunctions must involve a total spin of 1/2. The ion state spin eigenfunction corresponds to a linear combination of $\alpha(1)\alpha(2)\beta(3)$, $\alpha(1)\beta(2)\alpha(3)$ and $\beta(1)\alpha(2)\alpha(3)$ electron configurations only and therefore it can be said that only $\psi_j\alpha$ electron ionization from the orbital of interest contributes to the TMP corresponding to a doublet final ion state with a relative contribution of 2/3 (see Appendix A). Finally, the relative cross-sections for quartet and doublet (other than the HOMO) states must also allow for the double occupancies and respective degeneracies of the orbitals being ionized.

3.2. Cross-sections calculated using spin restricted open shell EMS theory

For spin restricted treatments of open shell systems such as O_2 the summation per electron in Eq. (2) is simply replaced by a multiplicative factor F equal to the relative intensity (see Appendix A). It should be noted that the factor F already includes the degeneracy and occupancy of the respective initial orbitals. Thus, the relative EMS cross-section can be written as:

$$\sigma_{\mathrm{EMS}} \propto F S_f^2 \int |\langle \boldsymbol{p}\Psi_f^{N-1}|\Psi_i^N\rangle|^2 \,\mathrm{d}\Omega \tag{5}$$

Using the THFA described above in Section 3.1, Eq. (5) simplifies to the following expression for spin restricted open shell Hartree–Fock orbitals $\psi_j(\boldsymbol{p})$:

$$\sigma_{\mathrm{EMS}} \propto F S_j^f \int |\psi_j(\boldsymbol{p})|^2 \,\mathrm{d}\Omega \tag{6}$$

Likewise, Eq. (5) simplifies within the TKSA (described above in Section 3.1) to the following expression involving spin restricted open shell Kohn–Sham orbitals $\psi_j^{\mathrm{KS}}(\boldsymbol{p})$:

$$\sigma_{\mathrm{EMS}} \propto F \int |\psi_j^{\mathrm{KS}}(\boldsymbol{p})|^2 \,\mathrm{d}\Omega \tag{7}$$

The same considerations regarding instrumental angular resolution effects described in Section 3.1 must also be taken into account before comparison of the spin restricted open shell calculations to experiment. The OVDs in Eq. (5) or MDs in Eqs. (6) and (7) are referred to as TMPs after momentum resolution folding.

In the spin restricted case, the relative intensity F for a given ion state with total spin S is proportional to the product of the spin degeneracy factor P_{spin} equal to $(2S+1)$ and orbital factor P_{orbit} equal to the orbital degeneracy of the ion state as has been pointed out in earlier photoelectron spectroscopy studies [42–44]:

$$F \propto P_{\mathrm{spin}} P_{\mathrm{orbit}} \tag{8}$$

It should also be noted that where several states arise from ionization of an orbital of an open-shell molecule (e.g. doublets and quartets for O_2), the sum of the F factors associated with the various final ion states arising

---

[2] It should be noted that in practice spin contamination can occur to varying extents in spin unrestricted treatments, see Section 4.1 below.

from a given orbital ionization must equal the number of electrons (occupancy) in that orbital [44]. This allows the intensities of the TMPs arising from ionization from the various orbitals of O_2 to be placed on a common scale. Thus, in constructing the spin-restricted TMPs corresponding to the $^2\Pi_g$, $^4\Pi_u$, $^2\Pi_u$, $^4\Sigma_g^-$, $^2\Sigma_g^-$, $^4\Sigma_u^-$ and $^2\Sigma_u^-$ final ion states of O_2 the relative intensity factors F of 2, 8/3, 4/3, 4/3, 2/3, 4/3 and 2/3, respectively, are used to put the TMPs on a common relative intensity scale.

4. Calculations

4.1. Hartree–Fock calculations

Spherically averaged theoretical momentum profiles have been calculated for the orbitals of O_2 using several basis sets of varying quality within the plane wave impulse and the target Hartree–Fock approximations (via Eq. (3) or Eq. (6)). Both the UHF (see Section 3.1) and ROHF (see Section 3.2) methods have been used for all basis sets. The instrumental angular (momentum) resolution was included in the calculations using the Gaussian-weighted planar grid method [41]. Various other calculated and experimental electronic properties are listed in Table 1. The experimentally derived equilibrium geometry for O_2 from Ref. [45] was used in the STO-3G-U, STO-3G-R, 6-311 + G*-U, 6-311 + G*-R, AUG5-U and AUG5-R calculations while the 168-U and 168-R calculations used the experimentally derived equilibrium geometry for O_2 from Ref. [46].

When considering the properties in Table 1, it should be noted that the UHF methods and ROHF methods give different values for the total energy and spin contamination. The highest orbital is partially filled in ROHF theory while all other electrons are spin-paired [50,51] (i.e. the α,β pairs have the same spatial orbital) so that ROHF calculations modify the closed-shell Hartree–Fock Hamiltonian only in the terms involving the unfilled outermost orbital. The UHF method, however, treats the effects of the unpaired electron on the α and β spin manifolds differently and thus assigns different spatial orbitals to all α and β electrons (i.e. two determinants are solved in the UHF method, one yielding a set of α molecular orbitals and the other yielding a set of β molecular orbitals, each with a possible occupancy of one). The increased flexibility of the UHF method causes the UHF total energy for a given molecule and basis set to be generally lower than the ROHF total energy. However, spin contamination can be problematic for UHF wavefunctions [50,51] and thus UHF wavefunctions are not true eigenfunctions of the total spin operator $\hat{S}^2$. A measure of the spin contamination is found by calculation of the expectation value of $\hat{S}^2$. The value of $\langle \hat{S}^2 \rangle$ is 2.0 for O_2 when no spin contamination is present and it can be seen that all the UHF calculations in Table 1 this value is exceeded due to interference from states of higher multiplicity. Spin contamination does not arise in the ROHF method and thus all ROHF calculations give an $\langle \hat{S}^2 \rangle$ value for O_2 of exactly 2.0. A large amount of spin-contamination in any wavefunction may cause inaccuracy in computed properties, but the spin contamination of the UHF wavefunctions in Table 1 is reasonably small ($< 3\%$).

Further details of the Hartree–Fock calculation methods and basis sets are described below. The total number of contracted Gaussian-type orbital functions (CGTO) used is also given. All calculations with the STO-3G, 6-311 + G* and AUG5 basis sets (described below) were done at the University of British Columbia with the Gaussian 92 program while the calculations with the 168-GTO basis set were done at Indiana University with the MELD program. Those calculations employing the UHF method have the '-U' extension added to the basis set symbol while the '-R' extension indicates the ROHF method.

4.1.1. (1u) STO-3G-U and (1r) STO-3G-R

These calculations employed a minimal basis set (effectively single zeta). Each function is a contraction of three Gaussian functions. The oxygen atoms have a (6s,3p)/[2s1p] contraction and thus 10 CGTO are used for O_2. This basis was designed by Pople and co-workers [52].

Table 1
Calculated and experimental properties for O_2 $X\,^3\Sigma_g^-$

	Basis set and calculation method[a]	Total energy (hartree)	$\langle \hat{S}^2 \rangle$	Θ_{zz} (au)[b]	$\langle r^2 \rangle_e$ (au)[c]	$p_{\max}$ (au)[d]
	Hartree–Fock calculations					
1u	STO-3G-U	−147.634	2.0034	−0.9307	40.652	1.36
1r	STO-3G-R	−147.632	2.0000	−0.9258	40.649	1.36
2u	6-311+G*-U	−149.660	2.0488	−0.4304	43.744	1.10
2r	6-311+G*-R	−149.638	2.0000	−0.4708	43.673	1.07
3u	AUG5-U	−149.686	2.0488	−0.1574	43.446	1.07
3r	AUG5-R	−149.663	2.0000	−0.2304	43.385	1.05
4u	168-U	−149.691	2.0484	−0.2178	43.446	1.07
4r	168-R	−149.667	2.0000	−0.2768	43.386	1.05
	Post-Hartree–Fock calculations					
4c	168-CI	−150.133	2.0000	−0.2766	43.337	1.03
4a	168-ACPF	−150.146	2.0000	−0.2716	43.410	1.03
	DFT calculations[e]					
3*l*	AUG5-L	−149.338	–	−0.3259	43.878	0.96
3p	AUG5-P	−150.547	–	−0.3390	43.924	0.95
3b	AUG5-BP	−150.418	–	−0.3224	43.708	0.98
	Experimental	−150.326[f]		−0.29[g]	44.4 ± 0.2[h]	1.0[i]

[a] Calculations performed at the experimental equilibrium bond length of 1.20748 Å (2.28181 au), Ref. [45] with the exception of the 168-U, 168-R, 168-CI and 168-ACPF calculations which were performed at the experimental equilibrium bond length of 1.20752 Å (2.28189 au), Ref. [46].

[b] The quadrupole moment is defined as $\Theta_{zz} = (1/2)\langle \Sigma q_i (3z_i^2 - r_i^2) \rangle$, summing over all nuclei and electrons. Calculated quadrupole moments are for a non-relativistic, non-vibrating, non-rotating molecule.

[c] The electronic spatial extent is defined as $\langle r^2 \rangle_e = \langle \Sigma r_i^2 \rangle$, summing over all electrons.

[d] The $p_{\max}$ corresponds to the value of momentum where the intensity of the momentum profile is at a maximum (see Fig. 4a and b).

[e] The total energy from Kohn–Sham DFT has been suggested to be in error because of shifted orbital energies relative to ionization potentials from Dyson's equation [33]. See also Section 4.3.

[f] The 'experimental' total energy is the estimated non-relativistic, non-vibrating, infinite nuclear mass total energy. Total energy obtained by adding the atomic energies from Ref. [47] to the D_0 values from Ref. [46] plus the zero point energy from the frequencies in Ref. [46].

[g] Recommended value from Ref. [48].

[h] Ref. [49].

[i] Present work.

4.1.2. (2u) 6-311 + G*-U and (2r) 6-311 + G*-R

These calculations used an augmented version of the 6-311G basis of Pople and co-workers [53]. The 6-311 + G* basis is formed by augmenting the 6-311G with diffuse s- and p-functions [54] and spherical d-type polarization functions [55] on the oxygen atoms to produce a (12s,6p,1d)/[5s,4p,1d] contraction per atom. A total of 44 CGTO are employed for O_2.

4.1.3. (3u) AUG5-U and (3r) AUG5-R

The basis set for these calculations was taken from the work of Dunning et al. [56–59]. The AUG5 basis set used in the present work is actually a truncated form of Dunning's aug-cc-pV5Z basis set in which all f-, g- and h-functions have been removed. This truncation was adopted to provide compatibility with the density functional calculations since the DFT program (deMon) cannot handle the higher *l* functions in its present form. Thus, the AUG5 consists of a (33s,13p,5d)/[7s,6p,5d] contraction per atom. In addition, the d functions have been changed from spherical to Cartesian so that the Hartree–Fock results from this basis set can be directly compared with the DFT results from this basis. Thus, a total of 110 CGTO are used for O_2.

4.1.4. (4u) 168-U and (4r) 168-R

The 168 CGTO basis set developed in the present work has a (19s,14p,3d,2f,1g)/[7s,8p,3d,2f,1g] contraction per atom. The primary (19s,14p) functions are taken from Partridge [60], while the (3d,2f,1g) polarization functions are from Dunning [56]. The first fourteen s functions were contracted into two s functions using the first fourteen 1s and 2s atomic orbital coefficients. Similarly, the first seven p functions are contracted into one p function using the first seven 2p atomic orbital coefficients. This contracted basis set is further augmented by additional diffuse s and p functions from Partridge's supplementary functions for $O^-(^2P)$ [60]. All components of the d, f and g functions are kept in the calculations.

4.2. MRSD-CI and ACPF calculations

4.2.1. (4c) 168-CI and (4a) 168-ACPF

The near Hartree–Fock limit 168-R calculation (described above in Section 4.1 for calculations 4u and 4r) was chosen as the initial reference calculation (thus all present CI calculations use the restricted open shell formulation). The frozen-core, multi-reference singles and doubles excitations configuration interaction (MRSD-CI) and average coupled-pair functional (ACPF) [31] calculations were then performed (at Indiana University with the MELD program) on both the neutral molecules and cation radicals with the neutral symmetry restricted ROHF K-orbitals [61]. The full ion-neutral overlap distributions were then calculated in the plane wave impulse approximation of the EMS cross-section via Eq. (5) to investigate the role of electron correlation and relaxation effects on the TMPs. The instrumental angular (momentum) resolution was included in the TMPs using the Gaussian-weighted planar grid method [41]. Various other electronic properties from these calculations are listed in Table 1. The experimentally derived equilibrium geometry for O_2 [46] was used in both calculations.

4.3. DFT calculations

4.3.1. (3l) AUG5-L, (3p) AUG5-P and (3b) AUG5-BP

The three density functional calculations were carried out using the deMon program [62,63] and the large AUG5 orbital basis set (described above in Section 4.1 for calculations 3u and 3r) at the experimental equilibrium geometry [45]. All calculations used a random extra-fine grid and the energy convergence was set at 10^{-7} hartree. The auxiliary basis set for fitting the charge density and exchange-correlation potential was the O(5,4;5,4) from the deMon program [62,63]. The AUG5-L calculation employs the local density approximation functional of Vosko et al. [64] while the AUG5-P calculation uses the gradient corrected correlation functional of Perdew and Wang [65,66]. The AUG5-BP uses a combination of the correlation functional of Perdew and Wang [65,66] and the exchange functional Becke [67]. The spin unrestricted Kohn–Sham orbitals have been extracted from the result and the TMPs have been calculated using the spin unrestricted TKSA equation for the EMS cross-section (Eq. (4)). The instrumental angular resolution effects [41] were also incorporated into the TMPs. Various other electronic properties from the DFT calculations are listed in Table 1. However, it should be noted that the use of inexact functionals in practical DFT calculations causes the total energies to differ from the exact result [33] and thus the DFT total energies in Table 1 are not readily comparable to those from Hartree–Fock methods, CI and ACPF. In addition, while the DFT calculations reported in the present work use the spin unrestricted open shell formulation and thus contain some degree of spin contamination, the $\langle \hat{S}^2 \rangle$ values are not tabulated in Table 1 because the deMon program does not compute this expectation value (see Section 4.1 for a discussion on spin contamination).

5. Results and discussion

5.1. Binding energy spectra

Oxygen belongs to the $D_{\infty h}$ point group and its (open-shell) ground state valence shell electronic configuration in the Hartree–Fock approximation is

$$\underbrace{2\sigma_g^2 2\sigma_u^2}_{\text{inner valence}} \qquad \underbrace{3\sigma_g^2 1\pi_u^4 1\pi_g^2}_{\text{outer valence}} \qquad X\,^3\Sigma_g^- \tag{9}$$

Removal of an electron from the valence orbitals give the following experimentally reported O_2^+ ionic states [2–10]:

$$\begin{array}{ll}
\textbf{configuration} & \textbf{ionic state} \\
2\sigma_g^2 2\sigma_u^2 3\sigma_g^2 1\pi_u^4 1\pi_g^1 & X\,^2\Pi_g \\
2\sigma_g^2 2\sigma_u^2 3\sigma_g^2 1\pi_u^3 1\pi_g^2 & a^4\Pi_u, A^2\Pi_u, {}^2\Pi_u(3) \\
2\sigma_g^2 2\sigma_u^2 3\sigma_g^1 1\pi_u^4 1\pi_g^2 & b^4\Sigma_g^-, B^2\Sigma_g^- \\
2\sigma_g^2 2\sigma_u^1 3\sigma_g^2 1\pi_u^4 1\pi_g^2 & c^4\Sigma_u^-, C^2\Sigma_u^- \\
2\sigma_g^1 2\sigma_u^2 3\sigma_g^2 1\pi_u^4 1\pi_g^2 & {}^4\Sigma_g^-, {}^2\Sigma_g^-, {}^4\Sigma_g^-(2), {}^2\Sigma_g^-(2)
\end{array} \tag{10}$$

In addition, a satellite peak of disputed origin has been observed at 33.0 eV (labelled Q in the present work).

The $X\,^2\Pi_g$ ground ionic state from $1\pi_g$ ionization has a vertical ionization potential of 12.30 eV and is well resolved in the measured photoelectron spectra [2–7]. The valence shell ionization potentials reported in the He(I) and He(II) studies of Edqvist et al. [3] and Baltzer et al. [6] and the XPS results of Siegbahn et al. [10] are presented in Table 2. Results from the earlier EMS study of Suzuki et al. [12] are also shown in Table 2.

Ionization from orbitals other than the $1\pi_g$ HOMO results in an ion with three singly occupied orbitals and

Table 2
Experimental ionization energies and peak widths[a] for O_2

Orbital origin[b]	Final ion state[b]	Vertical ionization energies					Peak width
		PES [3]	PES [6]	XPS [10]	EMS [12]	EMS this work[c]	EMS this work[d]
$1\pi_g$	$X\,^2\Pi_g$	12.30	12.31	13.1	12.5	12.30	0.80
$1\pi_u$	$a^4\Pi_u$	16.70	16.70	17.0	16.8	16.7	1.00
$1\pi_u$	$A^2\Pi_u$	17.73	17.64		16.8	17.5	0.90
$3\sigma_g$	$b^4\Sigma_g^-$	18.17	18.17	18.8	18.1	18.2	0.52
$3\sigma_g$	$B^2\Sigma_g^-$	20.43	20.30	21.1	20.3	20.3	0.70
$1\pi_u$	${}^2\Pi_u(3)$	24.0	23.9		23.7	23.7	1.50
$2\sigma_u$	$c^4\Sigma_u^-$	24.58	24.56	25.3	24.5	24.5	0.40
$2\sigma_u$	P,($C^2\Sigma_u^-$)		27.3	27.9	27.5	27.4	2.40
	Q			33.6	32.5	33.0	1.40
$2\sigma_g$	${}^4\Sigma_g^-$			39.6	39	38.9	2.25
$2\sigma_g$	${}^2\Sigma_g^-$			41.6	39	40.9	2.00
$2\sigma_g$	${}^4\Sigma_g^-(2)$			46	47	45.2	3.00
$2\sigma_g$	${}^2\Sigma_g^-(2)$			48	47	48.4	3.00

[a] All ionization energies and peak widths are in eV.

[b] Assignments from Refs. [3,4,6,10,12] with the exception of the peak at 33.0 eV which has been labelled Q in the present work.

[c] Energy position of the maximum of the Gaussian function width for this final ion state used in the deconvolution procedure.

[d] Natural half-width of the Gaussian function for this final ion state used in the deconvolution procedure.

thus both quartet and doublet ion states are observed. Ionization of the $1\pi_u$ orbital gives the $a^4\Pi_u$ state at 16.7 eV, the parent $A^2\Pi_u$ state at 17.6 eV and a higher energy $^2\Pi_u(3)$ pole at 23.9 eV [6]. The presence of a $^2\Pi_u(2)$ pole of very low intensity is predicted to be at ∼ 20 eV by theory [18,19,22,23]. This weak $^2\Pi_u(2)$ pole has not been identified experimentally [2–7]. It should be noted that other notation systems have been used for the predicted $^2\Pi_u(2)$ pole at ∼ 20 eV [18,19,22,23] and the experimentally observed $^2\Pi_u(3)$ pole at ∼ 23.7 eV. Baltzer et al. [6] employed a similar notation of 2 $^2\Pi_u$ and 3 $^2\Pi_u$ for these states, respectively, while Suzuki et al. [12] chose to ignore the predicted pole at ∼ 20 eV and instead applied the notation $^2\Pi_u(2)$ to their experimentally observed pole at 23.7 eV. Suzuki et al. [12] also assigned the peak at ∼ 33 eV in the EMS binding energy spectrum to $1\pi_u$ ionization and labelled the final ion state of this peak as $^2\Pi_u(3)$. In the present work, we label the peak at 33 eV simply as Q and discuss its possible orbital origin on the basis of the present experimental results and calculations in Section 5.2.4.

Table 3
MRSD-CI states and intensities (pole strengths) for O_2^+

State^2	Energy (au)	Energy (eV)	$(S_f^2)^a$	$(1.23\times S_f^2)^b$	Excitation	Coefficient
Σ_g^-	−149.3924	20.53	0.807	0.993	$(3\sigma_g)^{-1}$	0.91
	−148.9729	31.94	0.039	0.048	$(\pi_u)^{-1}(\pi_g)^{-1}(3\sigma_u)^1$	0.82
	−148.9360	32.94	0.020	0.025	$(\pi_u)^{-1}(2\sigma_u)^{-1}(\pi_g)^1$	0.80
	−148.9023	33.86	0.053	0.065	$(3\sigma_g)^{-1}(\pi_u)^{-2}(\pi_g)^2$	0.63
					$(\pi_u)^{-1}(2\sigma_u)^{-1}(\pi_g)^1$	0.53
	−148.6451	40.86	0.182	0.224	$(3\sigma_g)^{-1}(\pi_u)^{-2}(\pi_g)^2$	0.49
					$(2\sigma_g)^{-1}(2\sigma_u)^1(\pi_u)^{-1}(\pi_g)^1$	0.52
					$(2\sigma_g)^{-1}$	0.45
$^2\Sigma_u^-$	−149.2367	24.76	0.059	0.039	$(3\sigma_g)^{-1}(1\pi_u)^{-1}(1\pi_g)^1$	0.91
	−149.1290	27.69	0.270	0.332	$(3\sigma_g)^{-1}(1\pi_u)^{-1}(1\pi_g)^1$	0.74
					$(2\sigma_u)^{-1}$	0.55
	−148.9011	33.89	0.375	0.461	$(2\sigma_u)^{-1}$	0.61
					$(3\sigma_g)^{-1}(1\pi_u)^{-1}(1\pi_g)^1$	0.52
	−148.7611	37.70	0.029	0.036	$(1\pi_u)^{-2}(3\sigma_u)^1$	0.89
$^4\Sigma_u^-$	−149.2387	24.71	0.652	0.802	$(2\sigma_u)^{-1}$	0.84
	−149.1007	28.46	0.102	0.125	$(3\sigma_g)^{-1}(1\pi_u)^{-1}(1\pi_g)^1$	0.77
	−148.6945	39.52	0.025	0.031	$(3\sigma_g)^{-2}(3\sigma_u)^1$	0.71
	−148.5913	42.32	0.006	0.007	$(1\pi_u)^{-2}(2\sigma_u)^{-1}(1\pi_g)^2$	0.82
$^4\Sigma_g^-$	−149.4768	18.23	0.853	1.049	$(3\sigma_g)^{-1}$	0.92
	−149.0655	29.42	0.019	0.023	$(\pi_u)^{-1}(\pi_g)^{-1}(3\sigma_u)^1$	0.86
	−148.7941	36.81	0.009	0.011	$(\pi_u)^{-1}(2\sigma_u)^{-1}(\pi_g)^1$	0.66
					$(3\sigma_g)^{-1}(\pi_u)^{-2}(\pi_g)^2$	0.48
	−148.6705	40.17	0.773	0.951	$(2\sigma_g)^{-1}$	0.85
$^2\Pi_g$	−149.6947	12.30	0.815	1.002	$(1\pi_g)^{-1}$	0.91
	−149.2016	25.72	0.021	0.026	$(1\pi_u)^{-2}(1\pi_g)^1$	0.91
	−148.8933	34.11	0.011	0.014	$(1\pi_u)^{-2}(1\pi_g)^1$	0.80
$^2\Pi_u$	−149.4860	17.98	0.303	0.373	$(1\pi_u)^{-1}$	0.93
	−149.4366	19.16	0.004	0.005	$(1\pi_u)^{-1}$	
	−149.2561	24.23	0.477	0.587	$(1\pi_u)^{-1}$	0.73
	−148.8406	35.54	0.023	0.028	$(3\sigma_g)^{-1}(1\pi_g)^{-1}(3\sigma_u)^1$	0.59
					$(3\sigma_g)^{-2}(1\pi_u)^{-1}(1\pi_g)^2$	0.43
$^4\Pi_u$	−149.5291	16.81	0.838	1.031	$(1\pi_u)^{-1}$	0.94

[a] In the present work renormalized pole strengths are used when comparing with experiment, see discussion in Section 5.2.

[b] The renormalized pole strength is equal to $1.23\times S_f^2$. The factor of 1.23 is the scaling factor used to normalize the MRSD-CI calculation in Fig. 3a (see Section 5.2).

Ionization of a $3\sigma_g$ electron likewise leads to the separate quartet $b^4\Sigma_g^-$ and doublet $B^2\Sigma_g^-$ states which are observed in the photoelectron spectra at binding energies of 18.17 and 20.43 eV, respectively [3,4]. Similarly, removal of an electron from the inner closed shell $2\sigma_u$ orbital produces the O_2^+ $c^4\Sigma_u^-$ and $C^2\Sigma_u^-$ states. Baltzer et al. [6] have assigned these processes to ionization potentials of 24.56 eV and 27.3 eV, respectively. However, the present MRSD-CI results (Table 3) and other calculations [20–23] predict the presence of strong $^4\Sigma_u^-$ poles that overlap the peak traditionally associated with the $C^2\Sigma_u^-$ ionic state. This predicted dual character is supported by the present experiments and therefore we label the peak at 27.3 eV as peak P in the present work and discuss its composition in Section 5.2.4. The $^2\Pi_u(3)$ and $c^4\Sigma_u^-$ states are difficult to separate because of their closeness in energy. The observed ionization potentials for the peak corresponding to the $c^4\Sigma_u^-$ final ion state reported by high resolution experiments [3,6,7] are ~ 0.9 eV less than that reported in the XPS work of Siegbahn et al. [10].

Ionization of the inner-valence $2\sigma_g$ orbital produces the $^4\Sigma_g^-$ and $^2\Sigma_g^-$ states. Due to the more limited energy resolution of XPS, the vertical ionization potentials of these states are not as well-characterized as the lower energy states. Siegbahn et al. [10] reported $^4\Sigma_g^-$ and $^2\Sigma_g^-$ vertical ionization potentials of 39.6 and 41.6 eV, respectively, while Gardner and Samson [7] reported values of 39.7 and 40.3 eV. The threshold PES experiments of Ellis et al. [8] gave similar values of 39.5 and 40.8 eV. In addition, the pole strength of these states is thought to be further split into several satellite processes both from considerations of experiment [8,10–12] and theory [20–24]. The earlier studies [8,10–12] all showed that the inner valence region of the binding energy spectrum of O_2 is split into satellite peaks at ~ 46 and 48 eV. In Table 2, these states are labelled [12] as $^4\Sigma_g^-(2)$ and $^2\Sigma_g^-(2)$. However, additional satellite processes must occur since the intensity continues out to the limit of the data at 59 eV.

Fig. 1 shows the binding energy spectra of O_2 from 9 to 59 eV for measurements at relative azimuthal angles of (a) $\phi = 0.5°$ and (b) $\phi = 8.5°$ (impact energy of 1200 eV + binding energy) on a common intensity scale and at an energy resolution of 1.5 eV fwhm. Fig. 1c shows the summed binding energy spectra of O_2 from 9 to 59 eV for azimuthal ϕ angles of 0.5°, 1.5°, 3.5°, 5.5°, 8.5°, 9.5°, 12.5°, 13.5°, 16.5°, 17.5°, 20.5°, 24.5° and 30.5°. The energy scale was calibrated with respect to the $1\pi_g$ vertical ionization potential as measured by high resolution photoelectron spectroscopy [3,4]. Gaussian peak shapes have been fitted to the main peaks throughout the spectra in Fig. 1a–c using vertical ionization potentials and Franck–Condon widths (folded with the EMS instrumental energy width of 1.5 eV fwhm) estimated from photoelectron spectroscopy measurements [3,4,6,10]. The relative energy spacings of the Gaussian peaks were estimated from the vertical ionization potentials, with small adjustments to compensate for the asymmetries in the shapes of the Franck–Condon envelopes. For the states above 30 eV, energies and widths were more difficult to determine because of the lower energy resolution of the XPS studies [10]. Measured and calculated ionization potentials from the literature and those used in the present work are shown in Table 2. The peak widths used in the present work to fit the experimental EMS binding energy spectra in Fig. 1 are also given in Table 2.

In the outer valence region of the $\phi = 0.5°$ and 8.5° experimental binding energy spectra, several features can be seen in each spectrum. A peak due to the $1\pi_g$ ionization process (the $X\,^2\Pi_g$ state) is observed at a binding energy of 12.30 eV, which is consistent with the results of photoelectron spectroscopy [3,4,6]. This peak displays characteristic 'p-type' behaviour, having a greater intensity at $\phi = 8.5°$ than at $\phi = 0.5°$. The band from 15 to 21 eV contains four ionization processes. The quartet and doublet states arising from $1\pi_u$ ionization (the $a^4\Pi_u$ and $A^2\Pi_u$ states) are observed at 16.7 and 17.5 eV, respectively, in agreement with the observed PES spectrum [3,4,6]. These two states are clearly p-type and are difficult to deconvolute because of their close spacing [3,6] and because of the low intensity of the $A^2\Pi_u$ state. The next two quartet and doublet states ($b^4\Sigma_g^-$ and $B^2\Sigma_g^-$) arise from ionization of the $3\sigma_g$ orbital. The energies of these peaks are also consistent with the literature values of 18.17 and 20.43 eV [3,4,6]. The $b^4\Sigma_g^-$ state is very intense and 's-type' so that it has greater intensity at $\phi = 0.5°$ than at $\phi = 8.5°$. Thus, although the $b^4\Sigma_g^-$ state is very close to the $A^2\Pi_u$ state, the separation of the two states is aided in the EMS binding energy spectra by their different symmetries (i.e. s-type and p-type, respectively). Since the $B^2\Sigma_g^-$ state also arises from the $3\sigma_g$ orbital, it is likewise s-type.

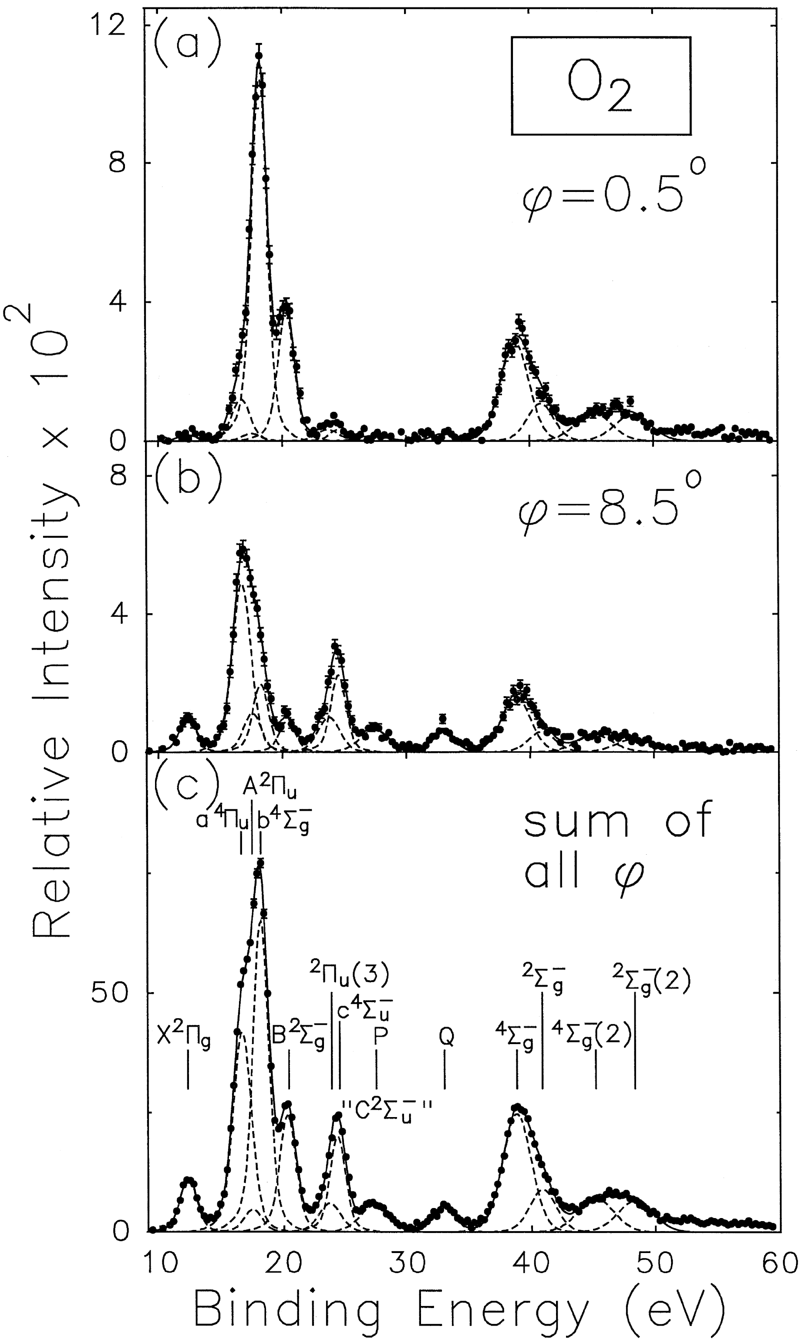

Fig. 1. EMS binding energy spectra of O_2 from 9 to 59 eV at (a) $\phi = 0.5°$, (b) $\phi = 8.5°$ and (c) over all thirteen ϕ angles, obtained at an impact energy of (1200 eV + binding energy). The dashed lines represent Gaussian fits to the peaks and the solid curve is the summed fit. See text for details.

The presence of the ${}^2\Pi_u(3)$ satellite peak arising from $1\pi_u$ ionization has been reported to be at 23.90 eV [6]. The EMS binding energy spectra and associated curve fit in Fig. 1 show a p-type momentum profile at an energy of 23.7 eV which can be identified with the ${}^2\Pi_u(3)$ satellite. This process is close in energy to the nearby $c^4\Sigma_u^-$ state at 24.56 eV [6] and it is clear from Fig. 1b that two ionization processes are present in this energy region. The $c^4\Sigma_u^-$ state arises from $2\sigma_u$ ionization and is also p-type. The closeness of these two states (and the fact that both are p-type) complicates the deconvolution of the spectrum in this region.

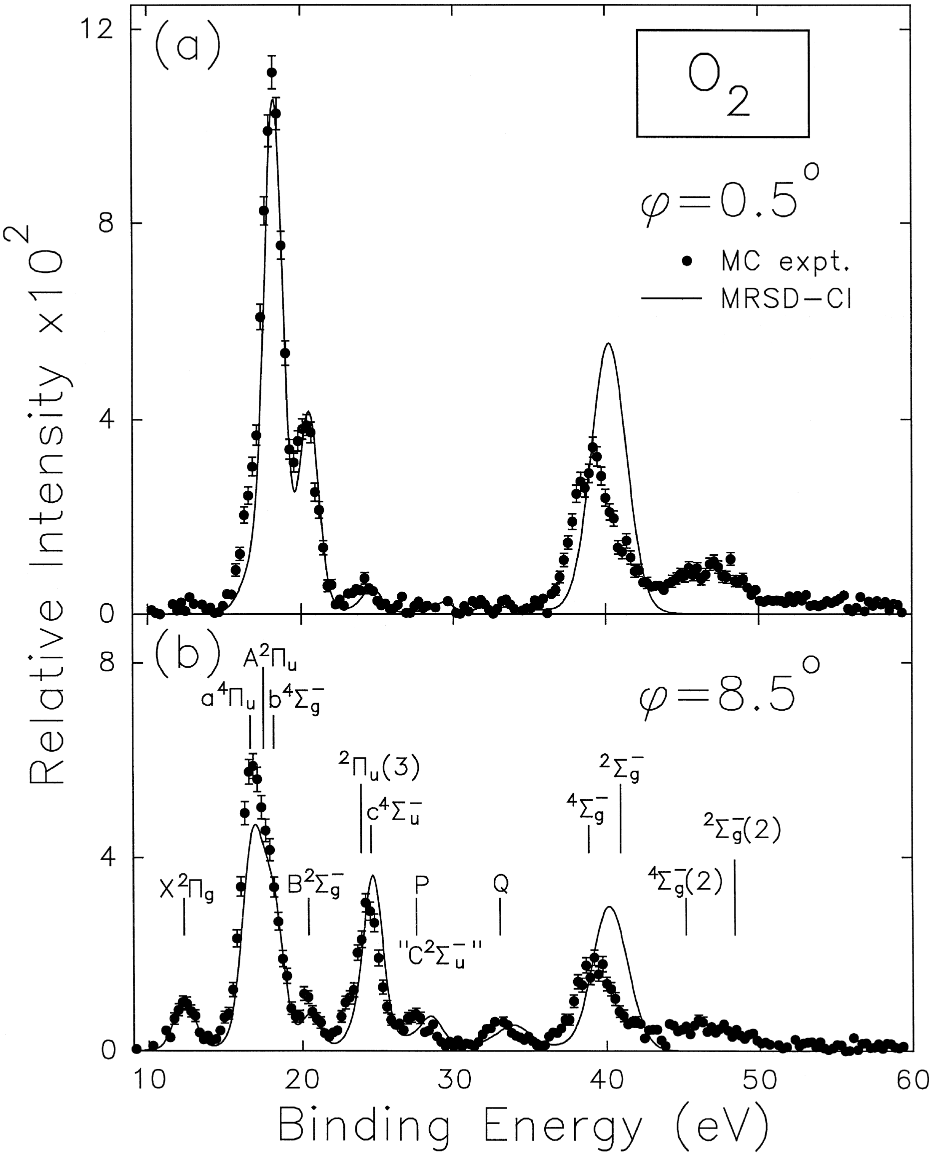

Fig. 2. Measured and calculated binding energy spectra of O_2 from 9 to 59 eV at (a) $\phi = 0.5°$ and (b) $\phi = 8.5°$. The solid curves indicate the synthesized theoretical binding energy spectra with pole energies and pole strengths (Table 3) given by the 168-CI MRSD-CI calculation which was also used for the angular dependence. The same energy peak widths as used in Fig. 1 have been folded into the synthesized spectra. The theoretical and experimental binding energy spectra are area normalized on the 9–36 eV region at $\phi = 8.5°$. See text for details.

A further ionization process, traditionally labelled [2–10] as the $C^2\Sigma_u^-$ state from $2\sigma_u$ ionization has been observed at 27.3 eV using high resolution photoelectron spectroscopy [6]. However, the present work (see Section 5.2.4 below) indicates that an additional ion state ($^4\Sigma_u^-$) contributes to the ionization in this energy region. In view of this situation the peak observed (Fig. 1) at 27.4 eV is referred to as peak P. In addition, the satellite peak labelled Q in the present work is observed at 33.0 eV in Fig. 1. The photoelectron study of Siegbahn et al. [10] gives a vertical ionization potential of 33.6 eV for this peak while the value of 32.5 eV from Suzuki et al. [12] is in better agreement with the present work.

The observed binding energy spectra (Fig. 1) in the high energy region from 36–59 eV are complex. An XPS study by Siegbahn et al. [10] assigned the broad peak at ~ 39 eV to contain the two $^4\Sigma_g^-$ and $^2\Sigma_g^-$ states from $2\sigma_g$ ionization at vertical ionization energies of 39.6 and 41.6 eV, respectively. However, it should be noted that energy positions are more difficult to determine with the lower energy resolution of XPS. Deconvolution of the EMS binding energy spectra in the present work gives slightly different results (Table 2) of 38.9 and 40.9 eV. Both states are clearly s-type, which is consistent with earlier EMS measurements [12]. Siegbahn et al. [10] also observed states in the high energy region at 46 and 48 eV which they assigned to be $^4\Sigma_g^-(2)$ and $^2\Sigma_g^-(2)$ satellite states from $2\sigma_g$ ionization. Suzuki et al. [12] supported this conclusion by measurement of the EMS momentum profiles. The EMS binding energy spectra in the present work also show intensity in this region and Gaussian peaks have been fitted to these dominantly s-type peaks at 45.2 and 48.4 eV (Table 2). In addition, the spectra in Fig. 1 show a high energy tail (mainly s-type) out to the limit of the data at 59 eV.

Calculated binding energy spectra are compared with the measured binding energy spectra in Fig. 2. Theory and experiment have been area normalized below 36 eV binding energy in the $\phi = 8.5°$ spectrum The calculated spectra are obtained by using the pole energies and pole strength S_f^2 values given by the presently reported 168-CI MRSD-CI calculation (see Table 3) as well as the angular dependence from the presently reported 168-CI theoretical momentum profiles for each pole at each angle. The measured EMS instrumental energy resolution function, as well as the widths of the transitions as observed in the experimental EMS binding energy spectra (see Fig. 1 and Table 2) have been folded into the calculated spectra. Good agreement is obtained between experiment and theory for the $1\pi_g$ HOMO orbital ($X\,^2\Pi_g$ final ion state). The correct shapes and positions are also reasonably well predicted at both angles for the band from 15 to 21 eV which contains four closely spaced ion states with two different symmetries. The intensity of the peak at ~ 20.5 eV corresponding to the $B^2\Sigma_g^-$ state (Table 2) is underestimated by theory at $\phi = 8.5°$ with the present normalization. In addition, the widths and positions in the 23–25 eV energy region are not well reproduced by theory (the closely-spaced $^2\Pi_u(3)$ and $c^4\Sigma_u^-$ states are observed in this region, see Fig. 1 and Table 2). The experimental and theoretical intensities for peaks P and Q observed experimentally at ~ 27.5 and ~ 33 eV are in agreement, but the energy positions predicted by theory are about 1 eV too high. Large discrepancies in energy positions and intensities also occur at both angles for the $^4\Sigma_g^-$ and $^2\Sigma_g^-$ states at ~ 39 eV. The difference in intensity between experiment and theory in this region can likely be attributed to the presence of higher energy satellite processes clearly visible in the experimental spectra out to the 59 eV limit not taken into account by the MRSD-CI calculation. The MRSD-CI calculation in the present work only takes into account states up to ~ 42 eV (see Table 3). In this regard, it should be noted that the MRSD-CI calculations are not expected to be accurate above the double ionization potential of O_2 (~ 36.3 eV) because of the presence of highly excited Rydberg states of O_2^+ converging on the double ionization limit.

5.2. Comparison of experimental and theoretical momentum profiles

Experimental and theoretical spherically averaged momentum profiles have been obtained for each of the valence orbitals of O_2. Experimental momentum profiles are extracted from the multichannel binning mode binding energy spectra. The relative intensities for the different transitions are maintained by the sequential, angular-correlated data collection process. The Gaussian fitting procedure, described above in Section 5.1 for the binding energy spectra, is used to determine the relative intensities of the various transitions at each

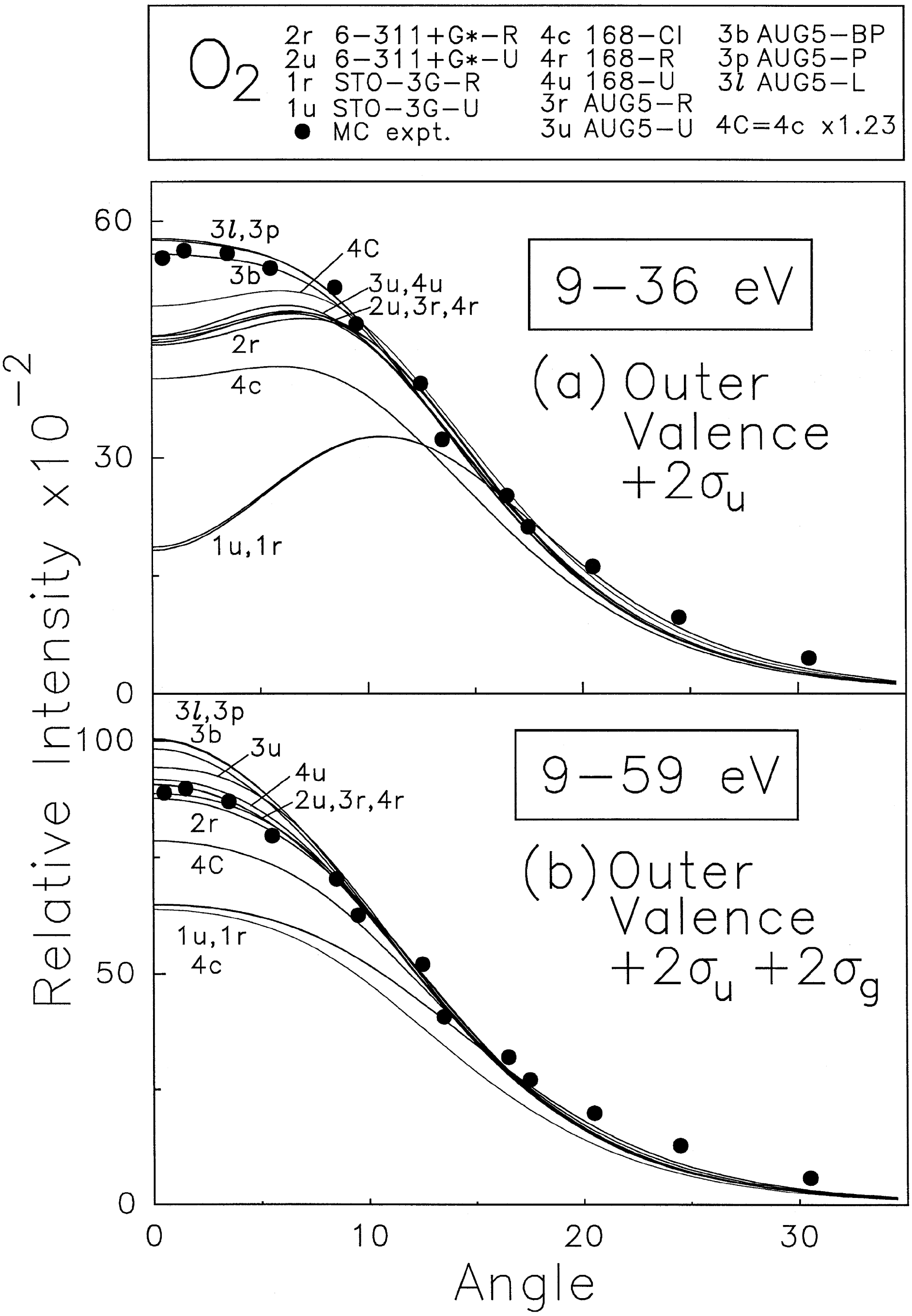

Fig. 3. Summed experimental and calculated spherically averaged momentum profiles for the (a) outer valence + $2\sigma_u$ orbital and (b) outer valence + $2\sigma_u$ + $2\sigma_g$ orbitals of O_2. The experimental data points are obtained by summing the measured binding energy spectra from 9 to 36 eV (Fig. 3a) and 9 to 59 eV (Fig. 3b) at each azimuthal angle (momentum). The solid curves are the sum of the respective momentum profiles calculated by several quantum mechanical methods and a wide variety of basis sets (see Section 4 for descriptions of the calculations). The momentum resolution has been folded into all calculations using the GW-PG method [41] before summation. The experimental data has been normalized to the AUG5-BP calculation in Fig. 3a and this same normalization factor has been applied to the data in Fig. 3b and all individual orbital momentum profiles (see Figs. 4–7). Note that the 168-CI calculation (curve 4c) is also shown as 1.23 × 4c (curve 4C). See text for details.

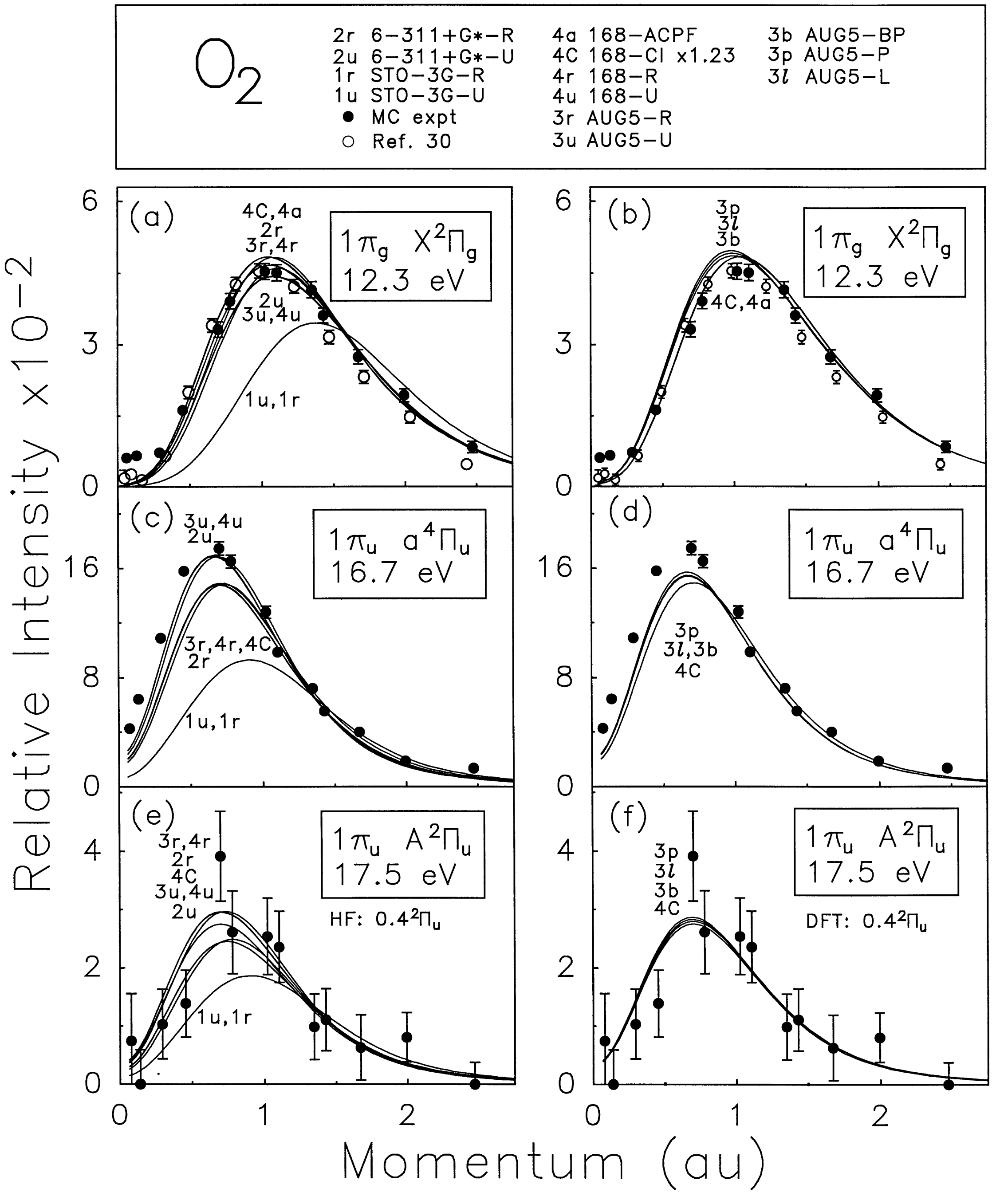

Fig. 4. Measured and calculated spherically averaged momentum profiles for the $1\pi_g$ ($X\,^2\Pi_g$) and $1\pi_u$ ($a^4\Pi_u$, $A^2\Pi_u$) orbitals of O_2. The solid circles represent the experimental energy dispersive multichannel measurements obtained in the present work with the binning mode of the EMS spectrometer. The open circles represent the experimental energy dispersive multichannel measurements from Ref. [30] obtained earlier in this laboratory using the non-binning mode of the same EMS spectrometer. All calculations have been spherically averaged and folded with the experimental momentum resolution. See text for details.

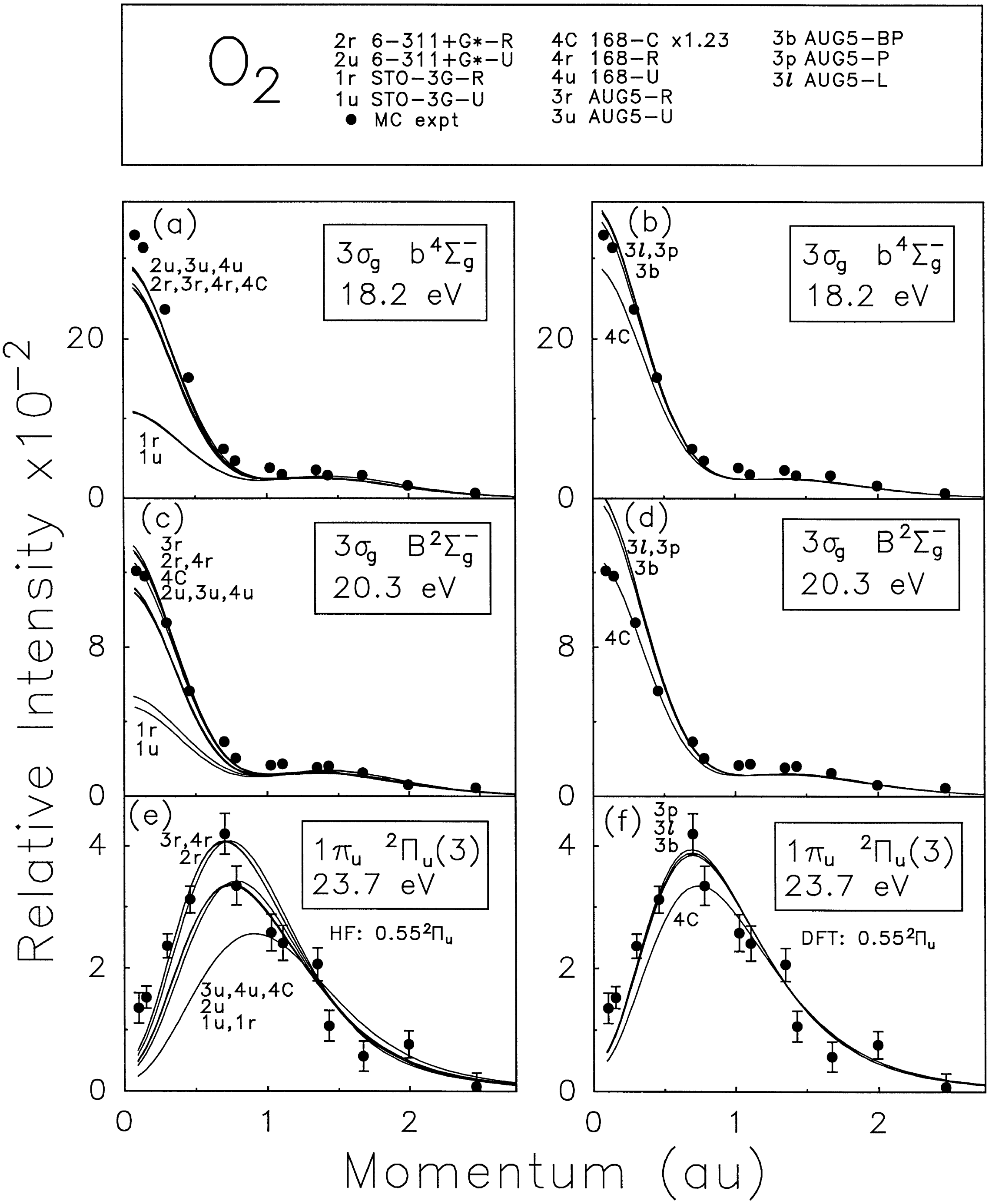

Fig. 5. Measured and calculated spherically averaged momentum profiles for the $3\sigma_g$ ($b^4\Sigma_g^-$, $B^2\Sigma_g^-$) and $1\pi_u$ ($^2\Pi_u(3)$) orbitals of O_2. The solid circles represent the experimental energy dispersive multichannel measurements obtained in the present work with the binning mode of the EMS spectrometer. All calculations have been spherically averaged and folded with the experimental momentum resolution. See text for details.

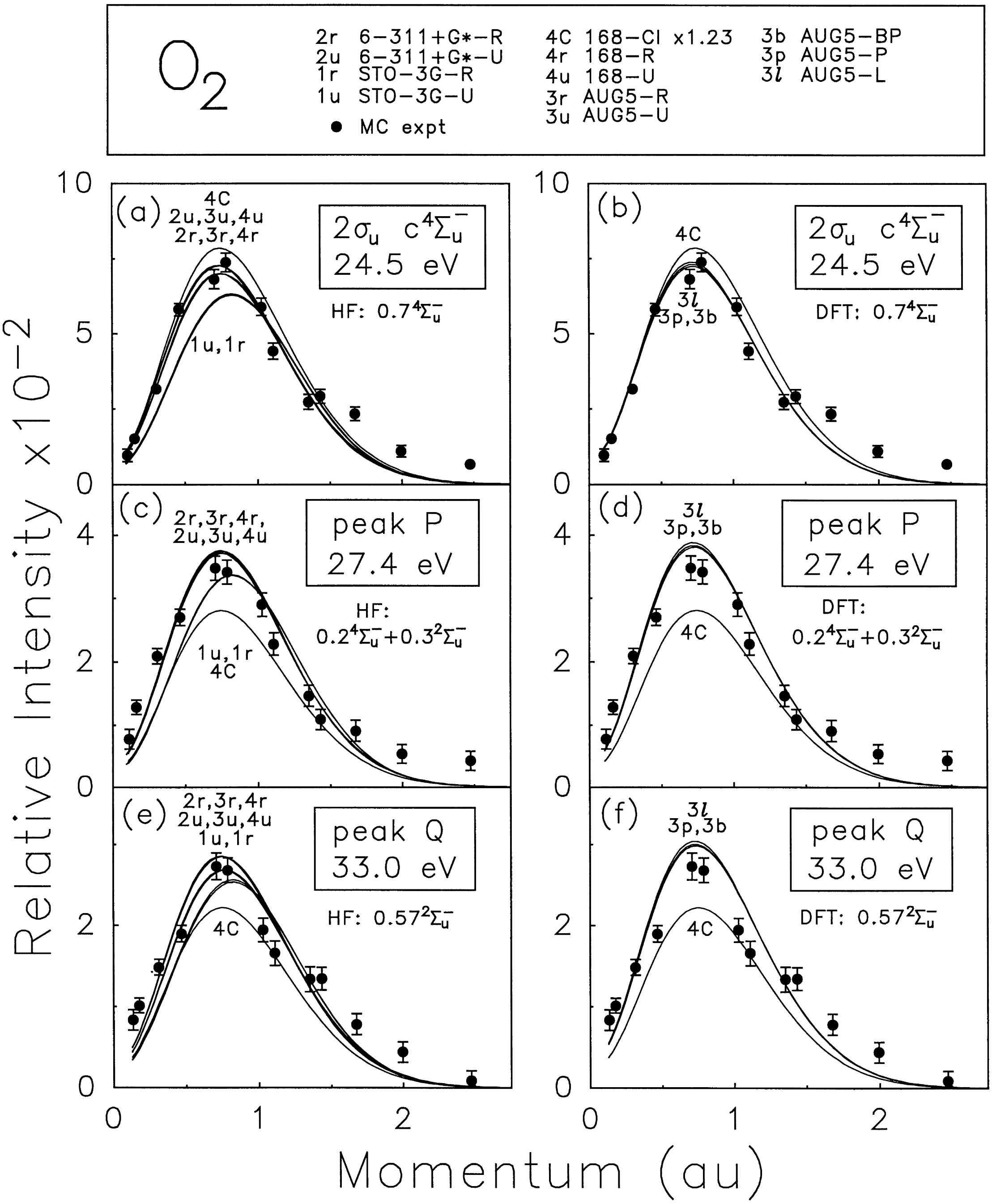

Fig. 6. Measured and calculated spherically averaged momentum profiles for the $2\sigma_u$ ($c^4\Sigma_u^-$, P and Q) orbital of O_2. The solid circles represent the experimental energy dispersive multichannel measurements obtained in the present work with the binning mode of the EMS spectrometer. All calculations have been spherically averaged and folded with the experimental momentum resolution. See text for details.

azimuthal angle ϕ. The experimental momentum profile corresponding to a particular final ion state is obtained by plotting the area under the corresponding fitted peak for each electronic state of the ion as a function of p (i.e. ϕ angle). With this procedure all experimental momentum profiles are automatically placed on a common relative intensity scale. The theoretical momentum profiles are obtained as described in Sections 3.1 and 3.2.

The experimental and theoretical momentum profiles (shown on an angle (ϕ) scale because of the wide range of binding energy included, see Eq. (1)) have been placed on a common intensity scale by normalizing the experimental data, summed from 9–36 eV, to the AUG5-BP theory summed over the outer valence orbitals ($1\pi_g$, $1\pi_u$, $3\sigma_g$) plus the $2\sigma_u$ orbital as shown in Fig. 3a. The $2\sigma_g$ orbital has been left out of the summation on Fig. 3a because:

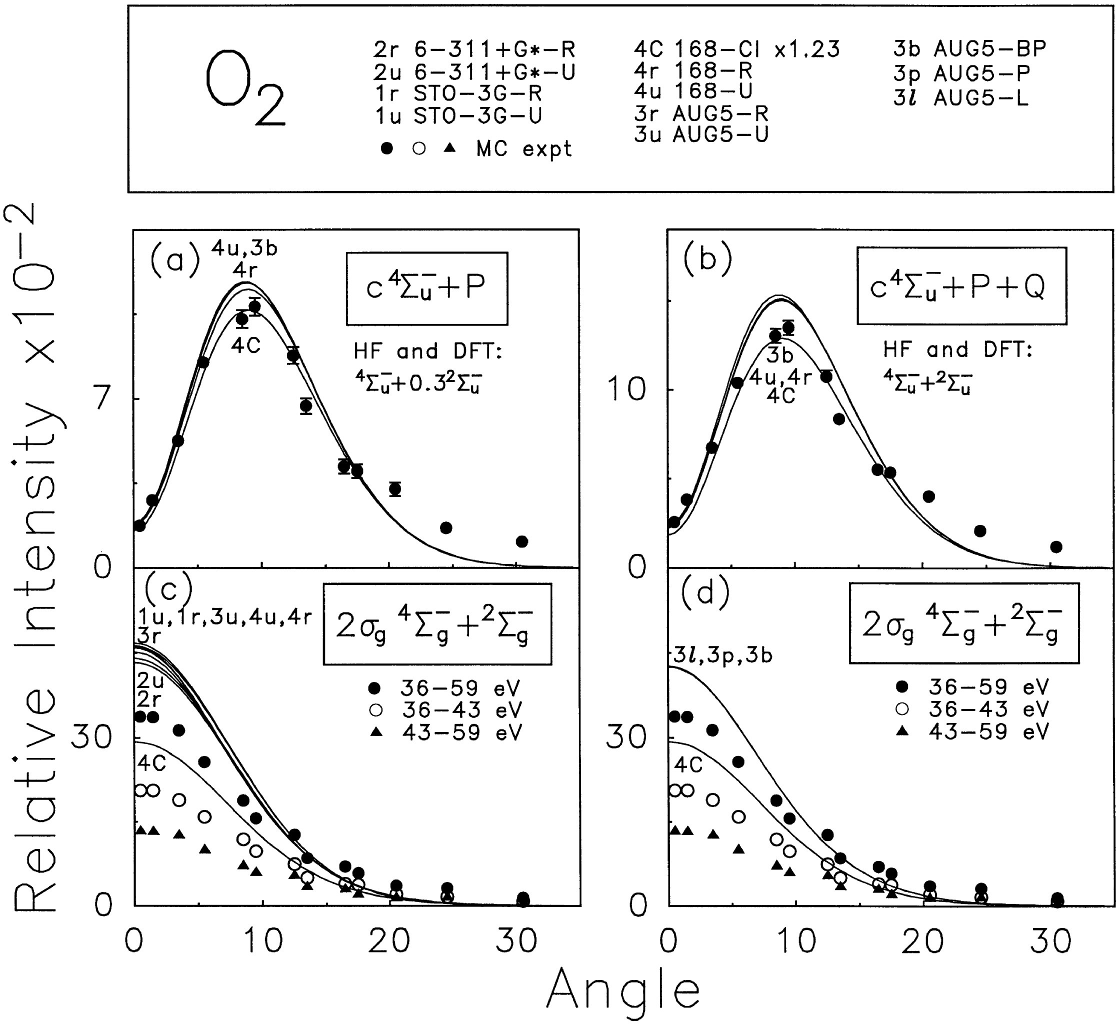

Fig. 7. Measured and calculated spherically averaged momentum profiles corresponding to sums of states as indicated and for the $2\sigma_g$ ($^4\Sigma_g^-$, $^2\Sigma_g^-$) orbital of O_2. The solid circles represent the experimental energy dispersive multichannel measurements obtained in the present work with the binning mode of the EMS spectrometer. All calculations have been spherically averaged and folded with the experimental momentum resolution. See text for details.

(1) As can be clearly seen on Fig. 1, there is apparently $2\sigma_g$ intensity beyond the limit of the experimental data which extends out to 59 eV.

(2) Little or no $2\sigma_u$ intensity is predicted [20–24] above 36 eV.

(3) The momentum profile analysis of the $2\sigma_u$ ionization processes giving $^4\Sigma_u^-$ and $^2\Sigma_u^-$ final ion states as shown in Figs. 6 and 7 and discussed in Section 5.2.4 below accounts for essentially all the intensity below 36 eV.

(4) This range is below the double ionization potential of O_2, see discussion in Section 5.1 above.

It should also be noted that all the TMPs in Fig. 3a are shown at unit pole strength except for the 168-CI momentum profile (curve 4c) which was constructed using the MRSD-CI poles in Table 3 each with their respective pole strength (S_f^2) value. It is clear from Fig. 3a that only the density functional theory calculations predict the correct shape of the observed XMP from 9–36 eV, especially in the low momentum region (below $\phi = 10°$). A shape very different from experiment is predicted at lower momenta (angles) by the Hartree–Fock and CI calculations. The AUG5-BP density functional theory calculation which includes both correlation and exchange has been chosen for normalization of the experimental data. However, the local (AUG5-L) and correlation-only (AUG5-P) density functional theory calculations give very similar results. The normalization factor obtained in the above procedure for Fig. 3a has been used for each individual orbital for all experimental and all theoretical comparisons (see Figs. 4–7) in the present work. The CI calculation (curve 4c) has much lower intensity than experiment because the chosen normalization to the AUG5-BP curve assumes that virtually all of the ionization intensity for the orbitals lies within the energy range 9–36 eV. The CI calculation however predicts typically only ~ 80% of each ionization manifold in the binding energy range below 36 eV (see Table 3) with the 'missing' pole strength unaccounted for and presumably located at higher binding energies. In order to treat the CI calculation in a manner consistent with the above normalization scheme, a second curve (4C, equal to $1.23 \times 4c$) has been constructed on Fig. 3a to provide the best intensity and shape fit between CI and experiment at least in the region above $\phi = 10°$. At lower ϕ angles the CI calculation provides a poor shape fit to experiment. It should be noted that this factor corresponds to the same normalization of CI to experiment as was used for the binding energy spectra in Fig. 2. Similarly, the summed experimental and theoretical momentum profiles over the entire measured binding energy range from 9–59 eV (Fig. 3b) for the valence orbitals ($1\pi_g$, $1\pi_u$, $3\sigma_g$, $2\sigma_u$ and $2\sigma_g$) have also been constructed using the same normalization factor for experiment and theory from Fig. 3a. The 168-CI momentum profile (curve 4c in Fig. 3b) was constructed using the MRSD-CI poles in Table 3 each with their respective S_f^2 value. Good agreement for shape is obtained between experiment and all calculations over the entire angular range of the data in Fig. 3b. Although the better Hartree–Fock calculations are close to the summed experimental data, the DFT calculations predict slightly greater intensity than experiment, particularly at the lower momenta. In this regard, additional extra $2\sigma_g$ intensity is expected above the upper limit of the experimental binding energy (59 eV) as discussed above. The discrepancy between theory and experiment above $\phi = 20°$ is likely due to distorted wave effects [15] at higher momenta. The 168-CI momentum profile predicts a lower intensity than experiment and this may be due to the remaining pole strength (S_f^2) which is likely located in the high energy range above 36 eV. In a manner similar to Fig. 3a, a second CI curve (4C) has been constructed by multiplying curve 4c by a constant scaling factor of 1.23. This curve matches the experiment better than curve 4c, although it still does not predict all the experimental intensity. The renormalized MRSD-CI pole strengths $(1.23 \times S_f^2)$ are also shown in Table 3.

The experimental and theoretical momentum profiles corresponding to each of the various ion states associated with the five valence orbitals of O_2 (see Section 5.1) are presented in Figs. 4–7 using the above normalization. The energies shown on Figs. 4–7 correspond to the binding energy peak maxima of the ion states observed in the present work (see Fig. 1 and also Table 2) The Hartree–Fock and DFT TMPs are presented at unit pole strength on Fig. 4a–d, 5a–d and 7b–d. In the other panels of Figs. 4–7, the Hartree–Fock and DFT TMPs are presented at a pole strength scaled by a factor to shape fit the XMP and to determine an experimental pole strength (the factor required in each case is indicated in each panel). The ACPF profile has only been calculated for the HOMO (see Fig. 4a and b) and is presented at unit pole strength. The MRSD-CI theoretical momentum profiles (curves 4C) in Figs. 4–7 are presented at their renormalized pole strengths ($1.23 \times S_f^2$) from Table 3.

5.2.1. The $1\pi_g$ orbital ($X\,^2\Pi_g$ final ion state)

The experimental momentum profile for the $1\pi_g$ (HOMO) orbital of O_2 ($X\,^2\Pi_g$ final ion state) is shown in Fig. 4a and b. The outermost XMP is well separated in energy from the rest of the valence ionization manifold, which ensures that all the observed intensity of the momentum profile is due to ionization to the lowest lying ion state only and contains no mixing with other ionization processes. The solid circles in Fig. 4a and b represent the experimental energy dispersive multichannel measurements obtained for the HOMO in the present work with the binning mode of the EMS spectrometer. The open circles in Fig. 4a and b represent the experimental energy dispersive multichannel measurements for the HOMO from obtained earlier [30] in this laboratory using the same EMS spectrometer in the non-binning mode. The HOMO data as originally published [30] was height normalized to CI and ACPF theory. In contrast, the present normalization is more stringent in that it has been achieved using theory and experiment summed over the outer valence plus the $2\sigma_u$ orbitals (see Fig. 3a and Section 5.2 above). Therefore, in Fig. 4a and b the earlier data [30] have been renormalized to the presently obtained measurements (solid circles) in the region of the maximum. With the presently employed more stringent normalization procedures, the comparison of theory and experiment is more rigorous than in the original work [30].

The $1\pi_g$ experimental momentum profile is compared on Fig. 4a with the various theoretical momentum profiles (TMPs) calculated at the UHF and ROHF Hartree–Fock level and also with the MRSD-CI and ACPF ion-neutral overlaps as described in Sections 4.1 and 4.2 above. Selected properties for each calculation and corresponding experimental values are shown in Table 1. The Hartree–Fock basis sets used range from a minimal STO-3G basis to the very much larger 168-GTO basis set. The calculated TMPs for the HOMO are as previously presented [30]. The effects of many-body correlation and electronic relaxation are also seen on Fig. 4a from the MRSD-CI and ACPF calculations of the TMPs. The 168-CI momentum profile in Fig. 4a corresponds to the $^2\Pi_g$ MRSD-CI pole at 12.30 eV (Table 3). The slightly higher cross-section than is expected from theory or symmetry considerations at very low p was persistently observed. The reason for this is not at present understood. Calibration using the Ar 3p orbital showed the expected nodal behaviour at the lowest momenta.

As might be expected, there is a large disagreement between the STO-3G minimal basis set calculations (curve 1u and 1r) and the observed shape and intensity of the XMP. The intermediate size basis set 6-311 + G*-U calculation (curve 2u) gives better agreement with experiment than the STO-3G calculations but it still underestimates the $p < 1$ au region of the XMP. The larger size basis set UHF calculations (curves 3u and 4u) are in better agreement with experiment with regard to shape and the similarity of curves 3u and 4u suggests that the UHF momentum profiles are essentially converged at this level of basis set size. Similarly, the higher level ROHF momentum profiles generally agree better with experiment as the basis set size is increased. As noted previously [30], the ROHF momentum profiles with intermediate and large size basis sets for this orbital generally display a higher relative intensity at low momentum than UHF calculations (of the same basis set size). The converged ROHF momentum profiles (curves 3r and 4r) match the shape and intensity of the XMP well but it should be noted that the UHF method predicts some other electronic properties (such as total energy, see Table 1) better than the ROHF method. It should be noted that, on the basis of the present normalization, the CI (curve 4C) and ACPF (curve 4a which is shown at unit pole strength) calculations fit the shape of the XMP comparably well and only slightly overestimate the intensity.

The density functional momentum profiles shown on Fig. 4b for the HOMO $1\pi_g$ orbital ($X\,^2\Pi_g$ final ion state) are the same as those published earlier [30]. It can be seen that all three DFT calculations give quite similar results and display slightly more intensity at low momentum than is observed experimentally. The MRSD-CI and ACPF calculations (curves 4C and 4a) most closely fit the experimental data for shape and intensity. However, all DFT calculations for the $1\pi_g$ orbital also provide a good description of the shape of the XMP.

5.2.2. The $1\pi_u$ orbital ($a^4\Pi_u$, $A^2\Pi_u$ and $^2\Pi_u(3)$ final ion states)

Experimental and theoretical momentum profiles for the $1\pi_u$ orbital of O_2 ($a^2\Pi_u$ final ion state) are shown in Fig. 4c and d. The best results for shape and intensity compared to the XMP are clearly the intermediate and large basis set UHF calculations of AUG5-U (curve 3u) and 168-U (curve 4u). The ROHF calculations from these basis sets are adequate for shape comparison, but the intensity is much too low. This is in contrast to the HOMO (Fig. 4a) and the previous work on the HOMOs of NO, O_2 and NO_2 [30] where ROHF calculations gave better shape comparisons with the XMP than UHF calculations. As noted above the 168-CI momentum profile in Fig. 4c and d corresponds to the $^4\Pi_u$ MRSD-CI pole predicted at 16.81 eV (Table 3). This 168-CI calculation predicts results (curve 4C) that are closer in intensity and shape to the intermediate and large basis sets ROHF results than UHF calculations. The DFT momentum profiles (Fig. 4d) are more intense than the 168-CI calculation (curve 4C), but are still unable to account for the experimental intensity at $p < 1.2$ au. The DFT momentum profiles predict the shape of the observed XMP well but not the intensity. If the density functional TMPs are multiplied by a factor of ~ 1.2, an excellent shape fit with experiment is obtained. The choice of functional has little effect on the overall shape of the TMPs.

Experimental and theoretical momentum profiles for the $1\pi_u$ orbital of O_2 corresponding to the $A^2\Pi_u$ final ion state are shown in Fig. 4e and f. The 168-CI momentum profile in Fig. 4e and corresponds to the $^2\Pi_u$ MRSD-CI pole at 17.98 eV (Table 3). The statistics for this final ion state are very limited due to the low intensity of this state and the difficulty in deconvoluting it from the energetically close and intense $a^4\Pi_u$ and $b^4\Sigma_g^-$ states. The Hartree–Fock and DFT theoretical momentum profiles in Fig. 4e and f have been further scaled by a factor of 0.4 to provide reasonable agreement with the intensity of the XMP and because of the additional $1\pi_u$ satellite intensity at higher energy discussed below (i.e. the $^2\Pi_u(3)$ peak at 23.7 eV). Within the rather limited precision of the experimental data, this experimentally obtained pole strength of 0.4 derived from a comparison of the intensities of the XMP and TMPs is consistent with the theoretical estimates of 0.44 by Cederbaum and Domcke [18], 0.34 by Dixon and Hull [19] and 0.35 by Honjou et al. [20,21]. The MRSD-CI calculation of the present work (see Table 3) predicts a renormalized pole strength of 0.373 in excellent agreement with the experimental value. It should also be noted that the ROHF momentum profiles in Fig. 4e generally predict more intense TMPs than their UHF counterparts. The 168-CI momentum profile (curve 4C) predicts a shape and intensity more similar to the ROHF limit curves 3r and 4r than the UHF limit curves 3u and 4u. The DFT momentum profiles (Fig. 4f) are very similar in shape and intensity to the 168-CI calculation.

The experimental and theoretical momentum profiles for the $1\pi_u$ orbital corresponding to the $^3\Pi_u(3)$ satellite state are shown in Fig. 5e and f. As expected, the XMP and TMPs are similar to the momentum profiles corresponding to the parent $A^2\Pi_u$ state at 17.5 eV (see Fig. 4e and f). It should also be noted that the 168-CI momentum profile in Fig. 5e and f corresponds to the $^2\Pi_u$ MRSD-CI pole at 24.23 eV (Table 3). The peak is of low EMS intensity and is close in energy to the peak corresponding to the $c^4\Sigma_u^-$ state and thus deconvolution leads to some scatter in the data. The satellite splitting has been accounted for by scaling the Hartree–Fock and DFT TMPs by a further factor of 0.55 to give the large basis set ROHF calculations (curves 3r and 4r) reasonable agreement with the experimental intensity. Other choices could be made for the normalization of experiment to theory, but curves 3r and 4r were chosen since ROHF momentum profiles agreed well for the intensities of other doublet states (see Fig. 4a and Fig. 5c). It should be noted that this experimentally derived pole strength of 0.55 is identical to the calculated pole strength reported by Cederbaum and Domcke [18]. The experimental pole strength from Fig. 5e and f also agrees quite well with the MRSD-CI calculation of the present work which predicts a renormalized $^2\Pi_u$ pole strength of 0.589 at 24.23 eV (see Table 3). Dixon and Hull [19] predicted a slightly higher pole strength of 0.64. On comparing the relative fits of the various TMPs in Fig. 5e and f, it is obvious that the minimal basis set STO-3G-U and STO-3G-R profiles are in poor agreement with the measured intensity and shape of the XMP. The large basis set UHF calculations (curves 3u and 4u) and the 168-CI calculation (curve 4C) predict reasonable shapes for the XMP, but have low intensity with the present normalization factor of 0.55. The DFT momentum profiles are all very similar and all fit the experiment well within the limited experimental statistics for this ionization process. The DFT momentum profiles adequately predict the experimental intensity in a manner similar to the large basis set ROHF calculations (curves 3r and 4r).

Previous work [12,25] assigned peak Q as $^2\Pi_u$ in character. However, a consideration of the theoretical and experimentally derived $^2\Pi_u$ pole strengths rules out the possibility that the 33 eV peak consists of $1\pi_u$ processes. The MRSD-CI theory of the present work (Fig. 2 and Table 3) predicts three $^2\Pi_u$ poles below ~ 24.3 eV. The MRSD-CI poles at 17.98 eV (renormalized pole strength 0.373) and 24.23 eV (renormalized pole strength 0.589) can be identified with the $A^2\Pi_u$ and $^2\Pi_u(3)$ states observed in the PES [3,4,6]. As mentioned previously, the $^2\Pi_u(2)$ state has not been observed experimentally but has been predicted to be formed with a very low cross-section at ~ 20 eV [18,19,22,23]. The weak $^2\Pi_u$ MRSD-CI pole at 19.16 eV in Table 3 (renormalized pole strength of 0.005) can be identified with this predicted $^2\Pi_u(2)$ state. The three MRSD-CI $^2\Pi_u$ energies and renormalized pole strengths (0.373, 0.005 and 0.589) below 24.3 eV in the present work are in reasonable agreement with previous predictions [18–21]. The propagator technique work of Cederbaum and Domcke [18] gave $A^2\Pi_u$, $^2\Pi_u(2)$ and $^2\Pi_u(3)$ energies of 17.47, 19.75 and 27.32 eV with relative intensities of 0.44, 0.01 and 0.55. The semi-empirical CI calculations of Dixon and Hull [19] predicted energies of 17.56, 19.97 and 22.72 eV with relative intensities of 0.34, 0.001 and 0.64. Honjou et al. [20,21] predicted energies of 17.84, 20.7 and 24.44 eV and relative intensities of 0.35, 0.000, and 0.47 for these states, respectively. In addition, Yeager and co-workers [22,23] obtained calculated ionization energies of 17.77, 20.82 and 24.56 eV for the $A^2\Pi_u$, $^2\Pi_u(2)$ and $^2\Pi_u(3)$ ionic states, respectively. It should be noted that all previous calculations [18–23] and the present MRSD-CI results place virtually all the $^2\Pi_u$ intensity below ~ 27.3 eV and, in most cases, below 24.5 eV. However, the $^2\Pi_u$ assignments of the previously published theory [18–23] and the presently reported calculation differ from those of Suzuki et al. [12] who designated the observed 23.7 eV peak as $^2\Pi_u(2)$ and then used this assignment to characterize the peak at ~ 33 eV as $^2\Pi_u(3)$ on the basis of the comparison of experimental intensity ratios with those from theory [18–21] and the theoretical study of Gerwer et al. [25]. It is suggested in the present work that the theoretical $^2\Pi_u$ intensity ratios were not compared with the correct experimental intensities in the previous EMS work [12] due to the predicted $^2\Pi_u(2)$ intensity at ~ 20 eV being incorrectly compared with the 23.7 eV experimental peak (and thus the theoretical $^2\Pi_u(3)$ intensity being incorrectly compared with the 33 eV experimental peak intensity). The ionization energies and pole strengths listed above from previously published theory [18–23], the MRSD-CI calculation of the present work and the photoelectron study by Baltzer et al. [6] all indicate that the peak at 23.7 eV in the EMS binding energy spectra should be assigned as $^2\Pi_u(3)$ and that no significant $^2\Pi_u$ intensity is present at 33 eV. The only predicted MRSD-CI $^2\Pi_u$ pole above 24.3 eV is of too low intensity (0.028 renormalized pole strength) and too high energy (35.54 eV) to account for peak Q. In addition, while Gerwer et al. [25] included the 33 eV peak in the total $1\pi_u$ photoionization cross-section for comparison of their theory to experiment, the agreement was only moderately good and several correction procedures were required for the summation of unresolved peaks in the dipole (e,2e) and line-source data. In the present work, the experimentally derived pole strengths for the peaks corresponding to the $A^2\Pi_u$ and $^2\Pi_u(3)$ states are found to be 0.4 and 0.55, respectively (Fig. 4e,f and Fig. 5e,f) and even with the limited statistics for these profiles these values correspond well with theory [18–21] and the presently reported MRSD-CI calculation. Thus, at least 0.95 of the experimental $^2\Pi_u$ pole strength has been accounted for at energies much lower than 33 eV and this represents essentially all the $^2\Pi_u$ pole strength, given the experimental statistics.

5.2.3. The $3\sigma_g$ orbital ($b^4\Sigma_g^-$ and $B^2\Sigma_g^-$ final ion states)

The experimental and theoretical momentum profiles for the $3\sigma_g$ orbital of O_2 ($b^4\Sigma_g^-$ final ion state) are shown in Fig. 5a and b. All profiles are similar in shape except that the STO-3G calculations (curves 1u and 1r) are in serious disagreement, as might be expected. The intermediate and large ROHF calculations (curves 2r, 3r and 4r) show much better agreement with the shape and intensity of the observed XMP than the STO-3G-R calculation. It should be noted that the 168-CI momentum profile in Fig. 5a and b corresponds to the $^4\Sigma_g^-$ MRSD-CI pole at 18.23 eV (Table 3). The MRSD-CI calculation (curve 4C) is formed from an initial ROHF reference state and thus the intensity of the 168-CI momentum profile is similar to curves 2r, 3r and 4r. Similar to the XMP corresponding to the quartet $(a^4\Pi_u)$ ionic state in Fig. 4c and d, the best fit to the shape and intensity of the XMP corresponding the quartet $b^4\Sigma_g^-$ ion state in Fig. 5a is given by the higher level UHF calculations (curves 2u, 3u and 4u). However, these UHF TMPs still underestimate the experimental intensity slightly. The high momentum region ($p > 1$ au) is modelled reasonably well by all calculations. Excellent agreement for both shape and intensity is obtained for the DFT and experimental momentum profiles (Fig. 5b). All the DFT profiles are very similar in shape and intensity and provide the best match to the experimental intensity.

The experimental and theoretical momentum profiles for the $3\sigma_g$ orbital of O_2 corresponding to the $B^2\Sigma_g^-$ final ion state are shown in Fig. 5c and d. Both the STO-3G-U and STO-3G-R momentum profiles are poor predictions of the XMP shape and intensity. The higher level UHF calculations (curves 2u, 3u and 4u) show reasonable agreement with the shape of the observed XMP but slightly underestimate its intensity. In contrast, the ROHF calculations (curves 2r, 3r and 4r) show excellent agreement with the experimental shape and intensity, particularly in the low momentum region. It appears that large basis set UHF calculations are best for predicting the shape and intensity of XMPs associated with quartet final ion states (Fig. 4c,d and Fig. 5a,b) while large basis set ROHF calculations are a better model for the XMPs corresponding to doublet final ion states (Fig. 4a,b and Fig. 5c,d). The 168-CI momentum profile (curve 4C) in Fig. 5c and d corresponds to the $^2\Sigma_g^-$ MRSD-CI pole at 20.53 eV (Table 3). This MRSD-CI momentum profile provides excellent agreement with the experimental shape and intensity of the XMP. The DFT momentum profiles are too intense (Fig. 5d) although the shape of the XMP is adequately predicted.

5.2.4. The $2\sigma_u$ orbital ($c^4\Sigma_u^-$ final ion state, peak P and peak Q)

The experimental and theoretical momentum profiles for the $2\sigma_u$ orbital of O_2 ($c^4\Sigma_u^-$ final ion state) are shown in Fig. 6a and b. The $^4\Sigma_u^-$ MRSD-CI pole at 24.71 eV (Table 3) has been chosen for the calculation of the 168-CI momentum profile (curve 4C). It is clear from Fig. 6a and b that the experimental and theoretical intensities are very different since the Hartree–Fock and DFT TMPs as shown have been multiplied by a factor of 0.7 to match the experimental intensity. This experimentally estimated pole strength of 0.7 is in good agreement with the (renormalized) pole strength of 0.802 at 24.71 eV calculated by the MRSD-CI method (Table 3). It is suggested that the ~ 30% difference in intensity between the TMPs and the XMP in Fig. 6a and b is due to splitting of the $2\sigma_u$ ionization process into additional $^4\Sigma_u^-$ satellite states or ‘poles’ due to electron correlation effects.

Considering next the broad peak Q at 33 eV, it should be noted that no $^4\Sigma_u^-$ states are predicted in this energy region by the present MRSD-CI calculations (see Table 3) or by any of the other earlier published theoretical studies [20–23]. It should also be noted that the region of the binding energy spectrum (Fig. 1) above 36 eV is dominantly due to s-type $(2\sigma_g)^{-1}$ processes as discussed in Section 5.1 and therefore any contributions from p-type processes (i.e. $^4\Sigma_u^-$ and $^2\Sigma_u^-$) in this region are very small or negligible. Peak Q must therefore contain essentially only $^2\Sigma_u^-$ states and a $0.57\,^2\Sigma_u^-$ fraction of the Hartree–Fock and DFT TMPs is found to fit the XMP for this peak (Fig. 6e and f). This fraction is in quite good agreement with the (renormalized) MRSD-CI $^2\Sigma_u^-$ pole strength of 0.461 predicted at 33.89 eV (Table 3). Honjou et al. [20,21] also predicted strong $^2\Sigma_u^-$ poles at 34.9 and 36.6 eV while Yeager and co-workers [22,23] identified the experimentally observed peak in the region of 33 eV with a $^2\Sigma_u^-$ ionization process calculated at 34.70 eV.

The above analysis leaves experimental pole strengths of $0.3\,^4\Sigma_u^-$ and $0.43\,^2\Sigma_u^-$ unaccounted for and this intensity must therefore be mostly in peak P at 27.4 eV since all other regions of the binding energy spectrum have been assigned (see Section 5.2.5 and Fig. 7 below for a discussion of the $(2\sigma_g)^{-1}$ contributions which are located above 36 eV). Peak P is well-fitted by the TMP linear combination of $(0.2\,^4\Sigma_u^- + 0.3\,^2\Sigma_u^-)$ as shown in

Fig. 6c and d. The above analysis of the $c^4\Sigma_u^-$ ionic state and peaks P and Q therefore account for $\sim 90\%$ $(0.7+0.2$ for $^4\Sigma_u^-$ and $0.57+0.3$ for $^2\Sigma_u^-)$ of the pole strength of the $^4\Sigma_u^-$ and $^2\Sigma_u^-$ manifolds. The above assignment of peak P is further supported by the present MRSD-CI and earlier calculations [20–23] which all predict both $^4\Sigma_u^-$ and $^2\Sigma_u^-$ ionization strength in the region of ~ 27 eV with relatively minor additional strength located in the higher energy region above 36 eV. Finally, it should be noted that 0.72 of the $^4\Sigma_u^-$ pole strength would be needed for a good fit if peak P was due to the quartet state and this is clearly not the case since ~ 0.7 of the $^4\Sigma_u^-$ pole strength is already contained in the $c^4\Sigma_u^-$ state at 24.5 eV.

Fig. 7a and b give further evidence that almost all of the $^4\Sigma_u^-$ and $^2\Sigma_u^-$ pole strength is accounted for if there are significant $^4\Sigma_u^-$ processes in peak P and if peak Q has mainly $^2\Sigma_u^-$ character. Fig. 7a shows the experimental data for the peak corresponding to the $c^4\Sigma_u^-$ ionic state (24.5 eV) and peak P (27.4 eV) added together and compared to several high-level calculated $2\sigma_u$ momentum profiles. The individual Hartree–Fock and DFT TMPs corresponding to $^4\Sigma_u^-$ final ion states are included in the sum with a unit pole strength while a pole strength of 0.3 has been used for the TMPs corresponding to $^2\Sigma_u^-$ final ion states. The CI calculation (curve 4C) in Fig. 7a consists of the summation of the poles at 24.71, 27.69 and 28.46 eV, each with their respective renormalized S_j^2 values. Good shape and intensity agreement is obtained for the TMPs and summed XMP in Fig. 7a, especially for the CI calculation. In Fig. 7b, the experimental data for the peak at 24.5 eV corresponding to the $c^4\Sigma_u^-$ ionic state, peak P (27.4 eV) and peak Q (33 eV) have been summed and compared to several high-level Hartree–Fock and DFT $2\sigma_u$ momentum profiles corresponding to $^4\Sigma_u^-$ and $^2\Sigma_u^-$ final ion states each with unit pole strength. The CI calculation (curve 4C) in Fig. 7b consists of the summation of the poles at 24.71, 27.69, 28.46 and 33.89 eV, each with their respective renormalized S_f^2 values. Within the statistics of the data it can be seen that experiment and theory are in good agreement for total intensity, indicating that essentially all of the $^4\Sigma_u^-$ and $^2\Sigma_u^-$ pole strength lies within the energy region containing the three peaks ($c^4\Sigma_u^-$, P and Q).

5.2.5. The $2\sigma_g$ orbital ($^4\Sigma_g^-$ and $^2\Sigma_g^-$ final ion states)

The experimental and theoretical momentum profiles for the $^4\Sigma_g^-$ and $^2\Sigma_g^-$ parent and satellite states from $2\sigma_g$ orbital ionization are shown in Fig. 7c and d. Siegbahn et al. [10] gave vertical ionization potentials of 39.6 and 41.6 eV for the $^4\Sigma_g^-$ and $^2\Sigma_g^-$ states, but the present EMS work gives slightly lower ionization potentials (Table 2). Gardner and Samson obtained ionization potentials of 39.7 and 40.4 for these states [7]. Due to the limited knowledge of the positions and widths of these states, an energy slice from 36–43 eV (open circles in Fig. 7c and d) encompassing the main peak centered at ~ 39 eV has been taken. The same normalization factor determined for all other orbitals (see Fig. 3) has been used in Fig. 7c and d. The MRSD-CI $^4\Sigma_g^-$ and $^2\Sigma_g^-$ poles at 40.17 and 40.86 eV (Table 3) have been chosen for the calculation of the 168-CI momentum profile (curve 4C) since their energies and pole strengths correspond most closely with the experimentally observed parent ion states. While the XMP is clearly s-type, it does not match the theoretical intensity and thus additional $2\sigma_g$ ionization intensity must occur in higher energy poles. All calculations (Hartree–Fock, MRSD-CI and DFT) model the experimental shape and intensity in a similar manner. A second energy slice from 43–59 eV (filled triangles in Fig. 7c and d) shows the same s-type shape and this is consistent with previous observations [10,12] indicating that the higher energy region is predominantly composed of $(2\sigma_g)^{-1}$ poles. The peak centered at ~ 47 eV accounts for the majority of the intensity in the 43–59 eV region (see Fig. 1) and the states assigned as $^4\Sigma_g^-(2)$ and $^2\Sigma_g^-(2)$ are found within this peak (see Refs. [10,12] and also Table 2). Results from the MRSD-CI calculation in the present work only extend to ~ 42 eV and do not take into account the very high energy region because of complications involving the modelling of double ionization. While the shape of the 36–59 eV

Fig. 8. Momentum and position density contour maps for the $1\pi_g$, $1\pi_u$ and $3\sigma_g$ orbitals of an oriented O_2 molecule calculated at the Hartree–Fock level using the 168-R basis set. The contour values represent 0.01, 0.03, 0.1, 0.3, 1.0, 3.0, 10.0, 30.0, and 99.0% of the maximum density. The side panels (top and right side) show the density along the dashed lines (dashed vertical and horizontal lines) for each density map.

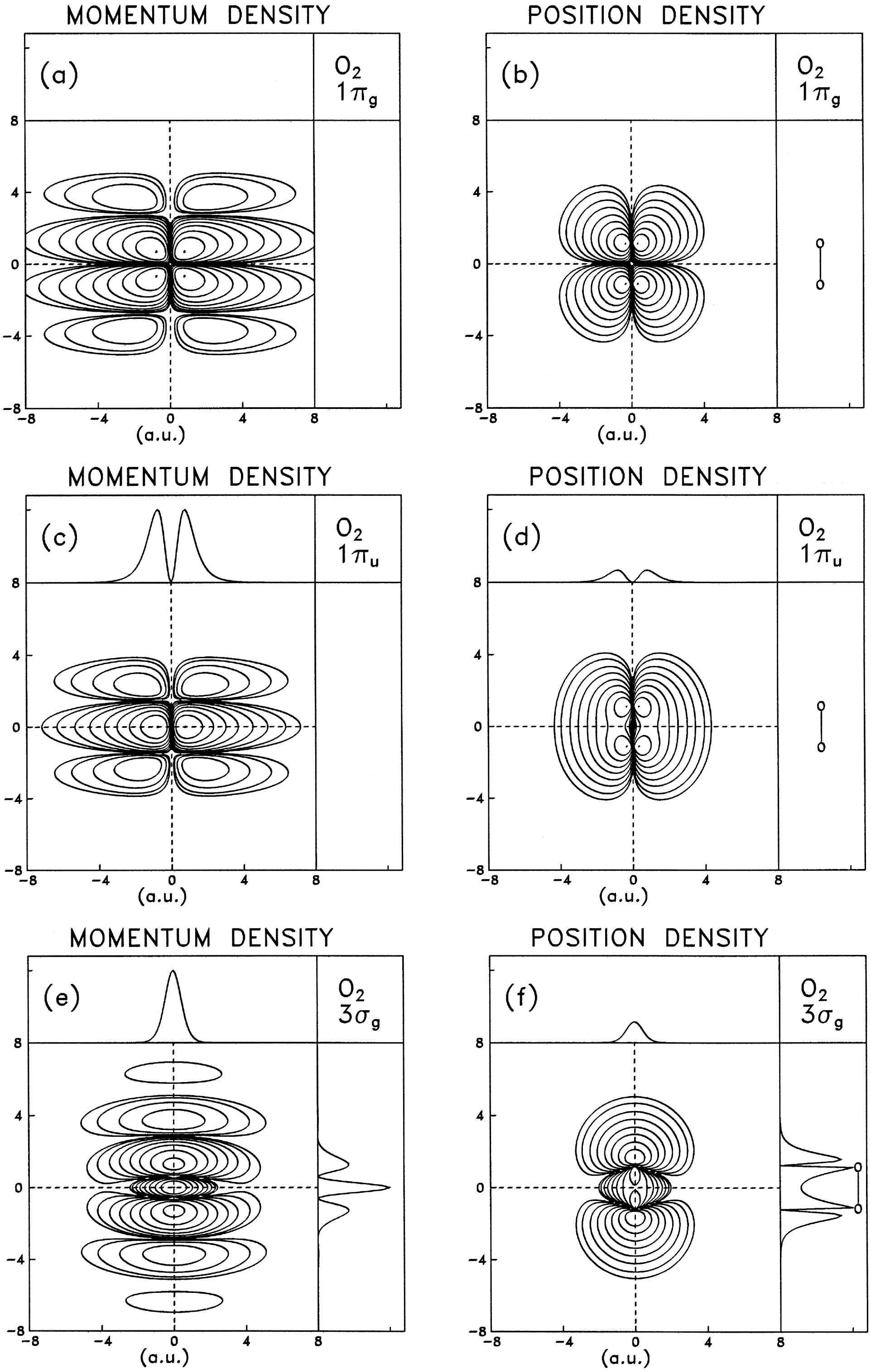
MOMENTUM DENSITY
(a)
O2
1πg
POSITION DENSITY
(b)
O2
1πg
MOMENTUM DENSITY
(c)
O2
1πu
POSITION DENSITY
(d)
O2
1πu
MOMENTUM DENSITY
(e)
O2
3σg
POSITION DENSITY
(f)
O2
3σg
8
4
0
−4
−8
−8
−4
0
4
8
(a.u.)

binding energy slice (filled circles in Fig. 7c and d) agrees well with that of the summed theory for $2\sigma_g$ ionization, some experimental intensity is apparently missing. However, as noted in Section 5.2, the missing intensity (Fig. 3) at a binding energy of 59 eV is still non-zero and therefore additional $2\sigma_g$ intensity remains at higher binding energies.

5.3. Density maps in momentum and position space

The momentum and position space density contour maps corresponding to each of the five valence orbitals of an oriented O_2 molecule are presented in Figs. 8 and 9. These density maps provide some insight into the corresponding (spherically averaged) experimental and theoretical momentum profiles. The position space maps are slices of the orbital electron density $|\psi|^2$ through a plane containing both nuclei. The momentum space

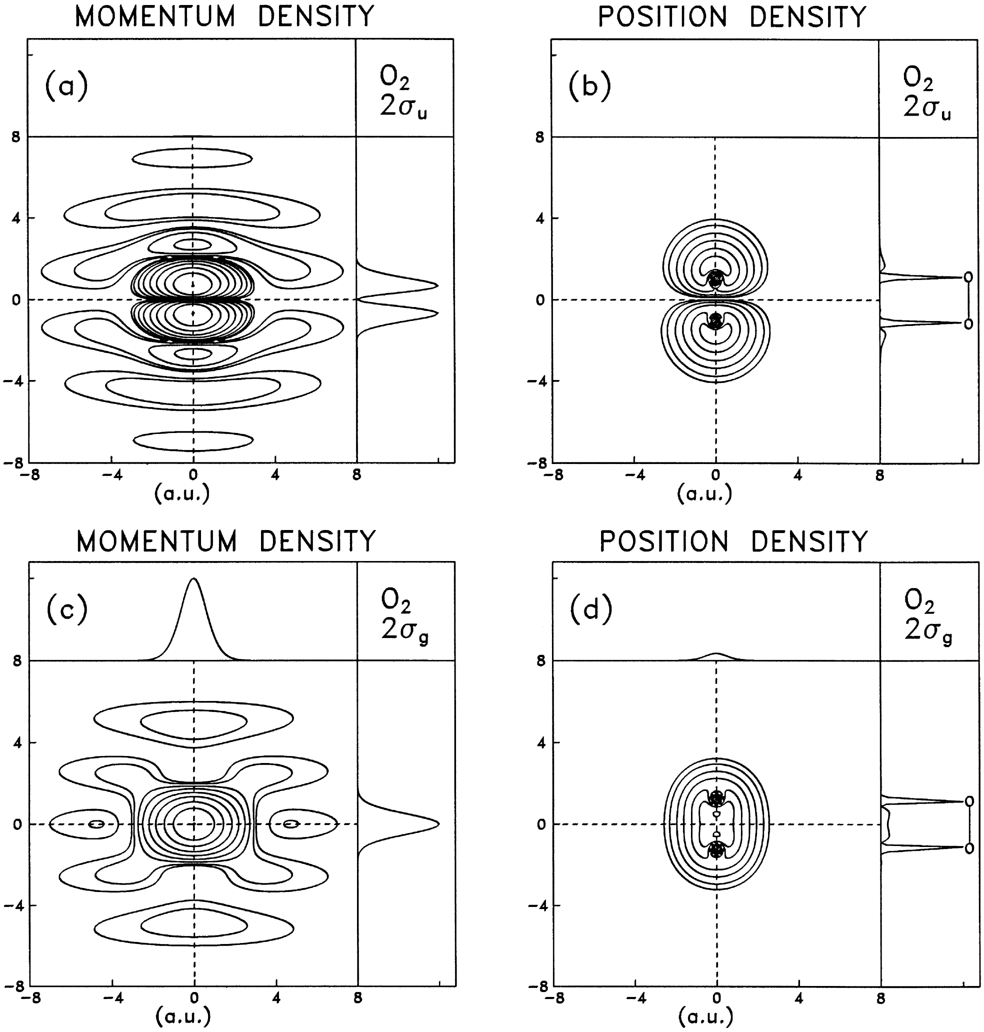

Fig. 9. Momentum and position density contour maps for the $2\sigma_u$ and $2\sigma_g$ orbitals of an oriented O_2 molecule calculated at the Hartree–Fock level using the 168-R basis set. The contour values represent 0.01, 0.03, 0.1, 0.3, 1.0, 3.0, 10.0, 30.0, and 99.0% of the maximum density. The side panels (top and right side) show the density along the dashed lines (dashed vertical and horizontal lines) for each density map.

maps show momenta perpendicular and parallel to the molecular plane. The calculations are based on the 168-R near Hartree–Fock limit results which have been found to provide generally good descriptions of the XMPs of O_2 at the Hartree–Fock level. The origin for the position space maps is the molecular center of mass and all dimensions are in atomic units. The side panels on each map show slices of the momentum or position space density along the vertical (right panel) and horizontal (top panel) dotted lines.

The momentum and position density maps for the $1\pi_g$ orbital of O_2 are shown in Fig. 8a and b. As discussed in previous work on the $1\pi_g$ density maps [30], simple molecular orbital Hartree–Fock models describe this MO as an antibonding π^* orbital involving out-of-phase (destructive interference) overlap of atomic O 2p orbitals. The expected shape of a pure π^* orbital can be seen from the r-map in Fig. 8b (i.e. four lobes of density and nodal planes both along the internuclear axis and perpendicular to the internuclear axis). The highly nodal character of this orbital in r-space is also reflected in p-space (r-space symmetry characteristics are conserved upon transformation to p-space and thus there are also two nodal planes in the p-map). In view of this high degree of nodal behaviour it is not surprising that the experimental and theoretical momentum profiles for this orbital display such a high p_{max} value of 1.0 au in view of the relation $p = \mathrm{i}\hbar\partial(\psi)/\partial x$ [68,69]. The interference of wavefunctions on the atomic centers is also reflected in the momentum density map as additional lobes called ‘bond oscillations’ [70–72].

The momentum and position density maps for the $1\pi_u$ orbital of O_2 are shown in Fig. 8c and d. The $1\pi_u$ orbital is a bonding orbital resulting from in-phase (constructive interference) side-on overlap of atomic O 2p orbitals. The expected two-lobed shape of the orbital can be seen from the r-map (Fig. 8d). Because the overlap is off the internuclear axis and because the lobes are of opposite sign, a nodal plane exists along this axis. Similarly, one nodal plane is observed in the p-map in the p_{parallel} direction (Fig. 8c). The momentum density at $p = 0$ is identically zero so that all (non-momentum resolution folded) profiles for this orbital have zero intensity at $p = 0$. The small intensity near $p = 0$ in the TMPs shown in Fig. 4a and b is due to momentum resolution folding effects.

The momentum and position density maps for the $3\sigma_g$ orbital of O_2 are shown in Fig. 8e and f. Constructive overlap of atomic orbital components is clearly seen in the region between the O atoms to produce a σ bond. The multiple lobes in the p-map are further evidence of this bonding behaviour. The large amount of momentum density at $p = 0$ (see top and side slices in the p-map) indicates the strongly s-type character of the experimental and theoretical momentum profiles for this orbital (see Fig. 5a–d). In addition, the small secondary maxima in the momentum density (see side slice in the p-map) are reflected in the spherically averaged momentum profiles as small p-type behaviour with maxima of $p \approx 1.4$ au.

The $2\sigma_u$ orbital of O_2 is predicted from molecular orbital theory to be antibonding and this is reflected by the momentum and position density maps for this orbital (Fig. 9a and b). The r-map displays a nodal plane perpendicular to the internuclear axis. Strong multiple lobes are observed in the p-map and no momentum density is observed at $p = 0$. Maxima in the momentum density observed at $p \approx 0.8$ au in the side slice of the p-map are reflected in the p-type shapes of the observed XMP and TMPs for this orbital.

The weakly bonding character of the $2\sigma_g$ orbital of O_2 is indicated by the σ density between the oxygen atoms in the r-map (Fig. 9c and d). The inner valence $2\sigma_g$ orbital is mostly composed of atomic-like O 2s character. On comparing with the density maps for the $3\sigma_g$ orbital (Fig. 8c and d) it is also clear that the $2\sigma_g$ is more spatially contracted (and tends to be more diffuse in momentum space) than the $3\sigma_g$ orbital. This is reflected by the broader momentum profiles for $2\sigma_g$ ionization in Fig. 7e and f than for the momentum profiles for $3\sigma_g$ ionization in Fig. 5a–d. The observed strongly s-type momentum profiles from $2\sigma_g$ ionization are also reflected by the presence of a large amount of momentum density in the $2\sigma_g$ p-map at $p = 0$.

Acknowledgements

Financial support for this work from the Peter Wall Institute for Advanced Studies is gratefully acknowledged. Financial support was also provided by the Natural Sciences and Engineering Research Council of

Canada (NSERC) and the National Science Foundation (USA). One of us (JR) gratefully acknowledges an NSERC Postgraduate Scholarship.

Appendix A. The EMS cross-section for the open shell molecule O_2—Contributions from the various final ion states

For an open shell molecule such as oxygen the EMS cross-sections for removal of α and β electrons are not identical (because different spatial orbitals are used in spin unrestricted calculations). In such cases the summations in Eqs. (2)–(4) must be taken into account.

Ionization from the $1\pi_g$ HOMO of O_2 is straightforward in that it can only involve removal of either of the two α electrons, leaving a doublet final ion state with a single unpaired α electron. Thus for the HOMO of O_2 the EMS cross-section is simply given by two times Eq. (2) or the appropriate THFA or TKSA representations (Eq. (3) or Eq. (4)) noting that the terms in $\psi_j(\boldsymbol{p})\beta$ or $\psi_j^{\mathrm{KS}}(\boldsymbol{p})\beta$ are not present). For example, in the THFA the HOMO cross-section becomes:

$$\sigma_{\mathrm{EMS}} \propto 2 S_j^f \int |\psi_{2\pi}(\boldsymbol{p})\,\alpha|^2 \,\mathrm{d}\Omega \tag{11}$$

In contrast, ionization from any orbital number j (i.e. ψ_j) of O_2 other than the HOMO results in an ion with three unpaired electrons leading to both quartet and doublet final ion states and the situation is therefore more complex. Let electrons 1 and 2 denote the electrons in the degenerate HOMO spatial orbitals ψ_1 and ψ_2, respectively. The spin eigenfunctions χ for the three electrons 1, 2 and j are given below for quartet and doublet final ion states, respectively:

Quartet final ion states

$$\begin{aligned}
&S=3/2, \quad M_S=3/2 && \chi_1=\alpha(1)\alpha(2)\alpha(j)\\
&S=3/2, \quad M_S=1/2 && \chi_2=\tfrac{1}{\sqrt{3}}\left[\alpha(1)\alpha(2)\beta(j)+\alpha(1)\beta(2)\alpha(j)+\beta(1)\alpha(2)\alpha(j)\right]\\
&S=3/2, \quad M_S=-1/2 && \chi_3=\tfrac{1}{\sqrt{3}}\left[\alpha(1)\beta(2)\beta(j)+\beta(1)\alpha(2)\beta(j)+\alpha(1)\beta(2)\beta(j)\right]\\
&S=3/2, \quad M_S=-3/2 && \chi_4=\beta(1)\beta(2)\beta(j)
\end{aligned} \tag{12}$$

Doublet final ion states

$$\begin{aligned}
&S=1/2, \quad M_S=1/2 && \chi_5=\tfrac{1}{\sqrt{6}}\left[2\alpha(1)\alpha(2)\beta(j)-\alpha(1)\beta(2)\alpha(j)-\beta(1)\alpha(2)\alpha(j)\right]\\
&S=1/2, \quad M_S=1/2 && \chi_6=\tfrac{1}{\sqrt{2}}\left[\alpha(1)\beta(2)\alpha(j)-\beta(1)\alpha(2)\alpha(j)\right]\\
&S=1/2, \quad M_S=-1/2 && \chi_7=\tfrac{1}{\sqrt{6}}\left[2\beta(1)\beta(2)\alpha(j)-\beta(1)\alpha(2)\beta(j)-\alpha(1)\beta(2)\beta(j)\right]\\
&S=1/2, \quad M_S=-1/2 && \chi_8=\tfrac{1}{\sqrt{2}}\left[\beta(1)\alpha(2)\beta(j)-\alpha(1)\beta(2)\beta(j)\right]
\end{aligned} \tag{13}$$

In an unrestricted open shell formulation the total antisymmetric wavefunctions for the oxygen ion (considering just the three electrons of interest) are formed by Slater determinants of the orbital functions ψ_1, ψ_2 and ψ_j and the above spin eigenfunctions. It should be noted that this treatment corresponds to an open shell target Hartree–Fock approximation (i.e. Eq. (3)). Analogous considerations will apply for open shells in CI or DFT treatments. The first ion total wavefunction is given by:

$$\Psi_1^{N-1}=\frac{1}{\sqrt{6}}\begin{vmatrix}\psi_1(1)\alpha(1) & \psi_2(1)\alpha(1) & \psi_j(1)\alpha(1)\\ \psi_1(2)\alpha(2) & \psi_2(2)\alpha(2) & \psi_j(2)\alpha(2)\\ \psi_1(j)\alpha(j) & \psi_2(j)\alpha(j) & \psi_j(j)\alpha(j)\end{vmatrix} \tag{14}$$

This total wavefunction and the other ion total wavefunctions can be written in shorthand form as:

Quartet final ion states

$$\begin{aligned}
\Psi_1^{N-1} &= \tfrac{1}{\sqrt{6}}\,|\psi_1\alpha\ \psi_2\alpha\ \psi_j\alpha| \\
\Psi_2^{N-1} &= \tfrac{1}{3\sqrt{2}}\left[|\psi_1\alpha\ \psi_2\alpha\ \psi_j\beta| + |\psi_1\alpha\ \psi_2\beta\ \psi_j\alpha| + |\psi_1\beta\ \psi_2\alpha\ \psi_j\alpha|\right] \\
\Psi_3^{N-1} &= \tfrac{1}{3\sqrt{2}}\left[|\psi_1\alpha\ \psi_2\beta\ \psi_j\beta| + |\psi_1\alpha\ \psi_2\beta\ \psi_j\alpha| + |\psi_1\alpha\ \psi_2\beta\ \psi_j\beta|\right] \\
\Psi_4^{N-1} &= \tfrac{1}{\sqrt{6}}\,|\psi_1\beta\ \psi_2\beta\ \psi_j\beta|
\end{aligned} \tag{15}$$

Doublet final ion states

$$\begin{aligned}
\Psi_5^{N-1} &= \tfrac{1}{6}\left[2|\psi_1\alpha\ \psi_2\alpha\ \psi_j\beta| - |\psi_1\alpha\ \psi_2\beta\ \psi_j\alpha| - |\psi_1\beta\ \psi_2\alpha\ \psi_j\alpha|\right] \\
\Psi_6^{N-1} &= \tfrac{1}{2\sqrt{3}}\left[|\psi_1\alpha\ \psi_2\beta\ \psi_j\alpha| - |\psi_1\beta\ \psi_2\alpha\ \psi_j\alpha|\right] \\
\Psi_7^{N-1} &= \tfrac{1}{6}\left[2|\psi_1\beta\ \psi_2\beta\ \psi_j\alpha| - |\psi_1\beta\ \psi_2\alpha\ \psi_j\beta| - |\psi_1\alpha\ \psi_2\beta\ \psi_j\beta|\right] \\
\Psi_8^{N-1} &= \tfrac{1}{2\sqrt{3}}\left[|\psi_1\beta\ \psi_2\alpha\ \psi_j\beta| - |\psi_1\alpha\ \psi_2\beta\ \psi_j\beta|\right]
\end{aligned} \tag{16}$$

Similarly, the total wavefunction for the ground state neutral molecule (considering just the four electrons of interest) can be written:

$$\Psi_i^N = \tfrac{1}{2\sqrt{6}}\,|\psi_1\alpha\ \psi_2\alpha\ \psi_j\alpha\ \psi_j\beta| \tag{17}$$

If the electron has been removed from the $\psi_j(\alpha)$ or $\psi_j(\beta)$ orbitals, the ion-neutral overlaps for quartet and doublet final ion states are as follows:

Quartet final ion states

$$\begin{aligned}
\langle\Psi_1^{N-1}|\Psi_i^N\rangle &= \tfrac{1}{12}\psi_j(\boldsymbol{p})\beta \\
\langle\Psi_2^{N-1}|\Psi_i^N\rangle &= \tfrac{1}{12\sqrt{3}}\,\psi_j(\boldsymbol{p})\alpha \\
\langle\Psi_3^{N-1}|\Psi_i^N\rangle &= 0 \\
\langle\Psi_4^{N-1}|\Psi_i^N\rangle &= 0
\end{aligned} \tag{18}$$

Doublet final ion states

$$\begin{aligned}
\langle\Psi_5^{N-1}|\Psi_i^N\rangle &= \tfrac{1}{6\sqrt{6}}\,\psi_j(\boldsymbol{p})\alpha \\
\langle\Psi_6^{N-1}|\Psi_i^N\rangle &= 0 \\
\langle\Psi_7^{N-1}|\Psi_i^N\rangle &= 0 \\
\langle\Psi_8^{N-1}|\Psi_i^N\rangle &= 0
\end{aligned} \tag{19}$$

Thus, the cross-section for quartet final ion states contains contributions from both Ψ_1^{N-1} and Ψ_2^{N-1}. The cross-section for doublet final ion states contains only the contribution from Ψ_5^{N-1}. Squaring the ion-neutral overlaps in Eqs. (18) and (19) gives the relative weights for these contributions (see below).

Within the Target Hartree–Fock Approximation (see Section 3.1), the spectroscopic strength for the cross-section per electron can be simplified as $S_f^2 = S_j^f$. Therefore, the relative intensities of the contributions to the quartet and doublet state cross-sections in the unrestricted case are (removing a common factor of 1/12) as follows:

Quartet final ion states

$$\sigma_{\mathrm{EMS}} \propto S_j^{(1)} \int |\psi_j(\boldsymbol{p})\beta|^2 \,\mathrm{d}\Omega + \tfrac{1}{3} S_j^{(2)} \int |\psi_j(\boldsymbol{p})\alpha|^2 \,\mathrm{d}\Omega \tag{20}$$

Doublet final ion states

$$\sigma_{\mathrm{EMS}} \propto \tfrac{2}{3} S_j^{(5)} \int |\psi_j(\boldsymbol{p})\alpha|^2 \,\mathrm{d}\Omega \tag{21}$$

It can be seen for the case of quartet final ion states that β and α electron ionization from orbital ψ_j contribute to the EMS cross-section by relative amounts of 1 and 1/3, respectively, assuming $S_j^{(1)} = S_j^{(2)}$. For the case of doublet final ion states, only α electron ionization from orbital ψ_j contributes to the EMS cross-section.

It should be noted that the target Kohn–Sham approximation is applied in the same manner as the THFA to yield equations for the oxygen EMS cross-section. These TKSA equations are the same as Eqs. (20) and (21) except that there are no spectroscopic factors S_j^f and $\psi_j(\boldsymbol{p})\alpha$ and $\psi_j(\boldsymbol{p})\beta$ are replaced with the corresponding momentum space Kohn–Sham spin orbitals $\psi_j^{\mathrm{KS}}(\boldsymbol{p})\alpha$ or $\psi_j^{\mathrm{KS}}(\boldsymbol{p})\beta$.

Turning now to a spin restricted open shell formulation, the values of $\int |\psi_j(\boldsymbol{p})\alpha|^2 \,\mathrm{d}\Omega$ and $\int |\psi_j(\boldsymbol{p})\beta|^2 \,\mathrm{d}\Omega$ are the same after spin integration. If it is assumed that all the S_j^f values in Eqs. (20) and (21) are the same, then these equations simplify to the following relations for the EMS cross-sections corresponding to formation of quartet and doublet final ion states from the same initial ROHF orbital:

Quartet final ion states

$$\sigma_{\mathrm{EMS}} \propto \tfrac{4}{3} \int |\psi_j(\boldsymbol{p})|^2 \,\mathrm{d}\Omega \tag{22}$$

Doublet final ion states

$$\sigma_{\mathrm{EMS}} \propto \tfrac{2}{3} \int |\psi_j(\boldsymbol{p})|^2 \,\mathrm{d}\Omega \tag{23}$$

Thus, the quartet and doublet final ion state cross-sections have relative intensities of 4/3 and 2/3 (i.e. they are in a 2:1 ratio). Therefore, for spin-restricted calculations, taking into account also the respective orbital occupancies and degeneracies, the resulting relative intensity factors for the open-shell molecule O_2 (i.e. 8/3 and 4/3 for $^4\Pi_{\mathrm{u}}$ and $^2\Pi_{\mathrm{u}}$ states, 4/3 and 2/3 for $^4\Sigma_{\mathrm{u,g}}$ and $^2\Sigma_{\mathrm{u,g}}$ states, and 2 for the special case of the $^2\Pi_{\mathrm{g}}$ state) are as described in the photoelectron spectroscopy literature [42–44] (i.e. the factors F derived in Section 3.2).

References

[1] D.F. Shriver, P.W. Atkins, C.H. Langford, Inorganic Chemistry, Freeman, New York, 1990.
[2] D.W. Turner, C. Baker, A.D. Baker, C.R. Brundle, Molecular Photoelectron Spectroscopy, Wiley, New York, 1970.
[3] O. Edqvist, E. Lindholm, L.E. Selin, L. Åsbrink, Phys. Scr. 1 (1970) 25.
[4] K. Kimura, S. Katsumata, Y. Achiba, T. Yamazaki, S. Iwata, Handbook of HeI Photoelectron Spectra of Fundamental Organic Molecules, Halsted Press, New York, 1981.
[5] J.A.R. Samson, J.L. Gardner, J. Chem. Phys. 67 (1977) 755.
[6] P. Baltzer, B. Wannberg, L. Karlsson, M. Carlsson Göthe, Phys. Rev. A 45 (1992) 4374.
[7] J.L. Gardner, J.A.R. Samson, J. Chem. Phys. 62 (1975) 4460.
[8] K. Ellis, R.I. Hall, L. Avaldi, G. Dawber, A. McConkey, G.C. King, J. Phys. B: Atom. Mol. Opt. Phys. 27 (1994) 3415.
[9] M.S. Banna, D.A. Shirley, J. Electron Spectrosc. Relat. Phenom. 8 (1976) 255.
[10] K. Siegbahn, C. Nordling, G. Johansson, J. Hedman, P.F. Heden, K. Hamrin, U. Gelius, T. Bergmark, L.O. Werme, R. Manne, Y. Baer, ESCA Applications to Free Molecules, North-Holland, Amsterdam, 1969.
[11] C.E. Brion, K.H. Tan, M.J. van der Wiel, Ph.E. van der Leeuw, J. Electron Spectrosc. Relat. Phenom. 17 (1979) 101.
[12] I.H. Suzuki, E. Weigold, C.E. Brion, J. Electron Spectrosc. Relat. Phenom. 20 (1980) 289.
[13] C.E. Brion, Int. J. Quant. Chem. 19 (1986) 1397.

[14] C.E. Brion, in: T. Anderson et al. (Eds.), The Physics of Electronic and Atomic Collisions, American Institute of Physics Press, New York, 1993, p. 350 and references therein.
[15] I.E. McCarthy, E. Weigold, Rep. Prog. Phys. 54 (1991) 789.
[16] K.T. Leung, in: Z.B. Maksic (Ed.), Theoretical Models of Chemical Bonding, Springer, Berlin, 1991.
[17] J.A. Tossell, J.H. Moore, M.A. Coplan, G. Stefani, R. Camilloni, J. Am. Chem. Soc. 104 (1982) 7416.
[18] L.S. Cederbaum, W. Domcke, Adv. Chem. Phys. 36 (1977) 206.
[19] R.N. Dixon, S.E. Hull, Chem. Phys. Lett. 3 (1969) 367.
[20] N. Honjou, K. Tanaka, K. Ohno, H. Taketa, Mol. Phys. 35 (1978) 1569.
[21] N. Honjou, K. Tanaka, K. Ohno, H. Taketa, Chem. Phys. 57 (1981) 475.
[22] J.A. Nichols, D.L. Yeager, P. Jørgenson, J. Chem. Phys. 80 (1984) 293.
[23] P. Swanstrom, J.T. Golab, D.L. Yeager, J.A. Nichols, Chem. Phys. 110 (1986) 339.
[24] G.D. Purvis, Y. Öhrn, J. Chem. Phys. 62 (1975) 2045.
[25] A. Gerwer, C. Asaro, B.V. McKoy, P.W. Langhoff, J. Chem. Phys. 72 (1980) 713.
[26] J.A.R. Samson, J.L. Gardner, G.N. Haddad, J. Electron Spectrosc. Relat. Phenom. 12 (1977) 281.
[27] E. Weigold, Y. Zheng, W. von Niessen, Chem. Phys. 150 (1991) 405.
[28] B.R. Todd, N. Lermer, C.E. Brion, Rev. Sci. Instrum. 65 (1994) 349.
[29] Y. Zheng, J.J. Neville, C.E. Brion, Y. Wang, E.R. Davidson, Chem. Phys. 188 (1994) 109.
[30] J. Rolke, N. Cann, Y. Zheng, B.P. Hollebone, C.E. Brion, Y.A. Wang, E.R. Davidson, Chem. Phys. 201 (1995) 1.
[31] J. Gdanitz, R. Ahlrichs, Chem. Phys. Lett. 143 (1988) 413.
[32] B.P. Hollebone, J.J. Neville, Y. Zheng, C.E. Brion, Y. Wang, E.R. Davidson, Chem. Phys. 196 (1995) 13.
[33] P. Duffy, D.P. Chong, M.E. Casida, D.R. Salahub, Phys. Rev. A 50 (1994) 4704, and references therein.
[34] M.E. Casida, Phys. Rev. A 51 (1995) 2005.
[35] Y. Zheng, J.J. Neville, C.E. Brion, Science 270 (1995) 5237.
[36] J.J. Neville, Y. Zheng, C.E. Brion, J. Am. Chem. Soc. 118 (1996) 10533.
[37] Y. Zheng, C.E. Brion, M.J. Brunger, K. Zhao, A.M. Grisogono, S. Braidwood, E. Weigold, S.J. Chakravorty, E.R. Davidson, A. Sgamellotti, W. von Niessen, Chem. Phys. 212 (1996) 269.
[38] J. Rolke, C.E. Brion, Chem. Phys. 207 (1996) 173.
[39] J. Rolke, Y. Zheng, C.E. Brion, S.J. Chakravorty, E.R. Davidson, I.E. McCarthy, Chem. Phys. 215 (1997) 191.
[40] A.O. Bawagan, C.E. Brion, E.R. Davidson, D. Feller, Chem. Phys. 113 (1987) 19.
[41] P. Duffy, M.E. Casida, C.E. Brion, D.P. Chong, Chem. Phys. 159 (1992) 347.
[42] P.A. Cox, F.A. Orchard, Chem. Phys. Lett. 7 (1970) 273.
[43] J.W. Rabalais, Principles of Ultraviolet Photoelectron Spectroscopy, Wiley, New York, 1977.
[44] J.H.D. Eland, Photoelectron Spectroscopy, Butterworths, London, 1984.
[45] E. Tiemann, J. Mol. Spectrosc. 91 (1982) 60.
[46] K. Huber, G. Herzberg, Constants of Diatomic Molecules, Van Nostrand Reinhold, New York, 1979, pp. 466–480.
[47] S.J. Chakravorty, S.R. Gwaltney, E.R. Davidson, Phys. Rev. A 47 (1993) 3649.
[48] D.E. Stogryn, A.P. Stogryn, Mol. Phys. 4 (1966) 371.
[49] Y. Zhang, A.W. Ross, M. Fink, Z. Phys. D 18 (1991) 163.
[50] I.N. Levine, Quantum Chem., 4th Ed., Prentice-Hall, Englewood Cliffs, 1991.
[51] L. Farnell, J. Pople, L. Radom, J. Phys. Chem. 87 (1983) 79.
[52] W.J. Hehre, R.F. Stewart, J.A. Pople, J. Chem. Phys. 51 (1969) 2657.
[53] R. Krishnan, M.J. Frisch, J.A. Pople, J. Chem. Phys. 72 (1980) 4244.
[54] T. Clark, J. Chandrasekhar, G.W. Spitznagel, P.v.R. Schleyer, J. Comp. Chem. 4 (1983) 294.
[55] M.J. Frisch, J.A. Pople, J.S. Binkley, J. Chem. Phys. 80 (1984) 3265.
[56] T.H. Dunning Jr., J. Chem. Phys. 90 (1989) 1007.
[57] R.A. Kendall, T.H. Dunning Jr., R.J. Harrison, J. Chem. Phys. 96 (1992) 6796.
[58] D.E. Woon, T.H. Dunning Jr., J. Chem. Phys. 98 (1993) 1358.
[59] D.E. Woon, T.H. Dunning Jr., J. Chem. Phys. 99 (1993) 1914.
[60] H. Partridge, Near Hartree–Fock quality GTO basis sets for the first- and third-row atoms. NASA Techn. Memorandum, 101044 (1989) pp. 73, 79, 85.
[61] D. Feller, E.R. Davidson, J. Chem. Phys. 74 (1981) 3977.
[62] A. St.-Amant, D.R. Salahub, Chem. Phys. Lett. 169 (1990) 387.
[63] D.R. Salahub, R. Fournier, P. Mlanarski, I. Papai, A. St.-Amant, J. Ushio, in: J. Labanowski, J. Andzelm (Eds.), Density Functional Methods in Chemistry, Springer, New York, 1991, p. 77.
[64] S.H. Vosko, L. Wilk, M. Nussair, Can. J. Phys. 58 (1980) 1200.
[65] J.P. Perdew, Phys. Rev. B 33 (1986) 8822.
[66] J.P. Perdew, Y. Wang, Phys. Rev. B 33 (1986) 8800.

[67] A.D. Becke, Phys. Rev. A 38 (1988) 3098.
[68] C.E. Brion, J.P.D. Cook, I.G. Fuss, E. Weigold, Chem. Phys. 64 (1982) 287.
[69] A.O. Bawagan, C.E. Brion, M.A. Coplan, J.A. Tossell, J.H. Moore, Chem. Phys. 110 (1986) 153.
[70] J.P.D. Cook, C.E. Brion, J. Electron Spectrosc. Relat. Phenom. 15 (1979) 233.
[71] K.T. Leung, C.E. Brion, Chem. Phys. 82 (1983) 113.
[72] J.R. Epstein, A.C. Tanner, Compton Scattering, in: B.G. Williams (Eds.), McGraw-Hill, New York, 1997, p. 209.